

Technical Design Report of the CEPC Reference Detector

Technical Design Report of the CEPC Reference Detector

Author: the CEPC study group

Institute:

Date: June 9, 2025

Version: 0.1 build: 2025-05-13 00:36:08Z

Bio: Information

Contents

Chapter 1 Hadronic calorimeter	1
1.1 Overview	1
1.2 Design	2
1.2.1 Overall design	2
1.2.2 Single layer structure	3
1.2.3 Barrel	3
1.2.4 Endcap	6
1.2.5 Connection to other detectors	8
1.2.6 Summary	9
1.3 Key technologies and major challenges	9
1.4 Past R&D to demonstrate technologies and prototypes	10
1.4.1 Glass scintillator	11
1.4.1.1 Light yield	11
1.4.1.2 Light attenuation length	13
1.4.1.3 Radiation resistance	15
1.4.2 Photon detector	17
1.4.3 Simulation study of attenuation length	18
1.4.4 Measurements of GS with SiPM	20
1.4.5 Calibration	22
1.4.5.1 Calibration using physics processes	22
1.4.5.2 Hardware calibration	22
1.4.6 Readout electronics for R&D	23
1.4.7 Prototype	25
1.4.7.1 Simulation of GS-HCAL prototype	25
1.4.7.2 Design and construction plan of GS-HCAL prototype	26
1.4.7.3 Beam test consideration	27
1.5 Simulation and performance	28
1.5.1 Simulation and digitization	28
1.5.2 Single hadron energy resolution	28
1.5.3 Understanding of large constant term	29
1.5.4 Performance	31
1.6 Alternative solutions	31
1.6.1 Study of SDHCAL	32
1.6.2 Study of AHCAL	34
1.7 Summary and future plan	38
1.8 Cost table and justification	38
References	39

Chapter 1 Hadronic calorimeter

1.1 Overview

Hadronic calorimeter (HCAL) is employed in the CEPC detector system to provide an energy measurement of hadronic jets with excellent resolution and hermetic coverage. To fully exploit the potential of physics program for Higgs and electroweak physics, all possible final states from decays of intermediate vector bosons, Z, W and the Higgs boson need to be reconstructed and well identified with high sensitivity. In particular, to clearly identify hadronic final states of $H \rightarrow ZZ^* \rightarrow 4j$ and $H \rightarrow WW^* \rightarrow 4j$, the energy resolution of the calorimetry for hadronic jets needs to be pushed beyond today's limit. In order to distinguish the hadronic decays of W and Z bosons, a 3-4% invariant mass resolution for two-jet system is required. Such a performance needs a jet energy resolution of $30\%/\sqrt{E}$ at energies below 100 GeV as shown in Figure 1.1. This would be about a factor of two better than that of the LEP detectors and the currently operating LHC detectors, which is a very challenging performance to achieve.

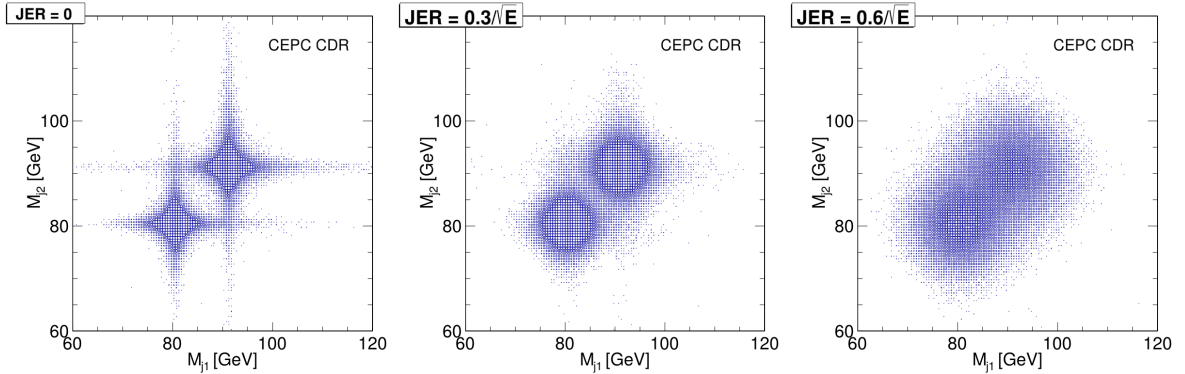


Figure 1.1: Separation of W and Z bosons in their hadronic decays with different jet energy resolutions: $0\%/\sqrt{E}$ (left plot), $30\%/\sqrt{E}$ (middle plot), $60\%/\sqrt{E}$ (right plot). A jet energy resolution of $30\%/\sqrt{E}$ is required to well separate the hadronic decays of W and Z bosons.

Two different technology approaches are pursued for the calorimetry system, the first one aiming to measure individual particles in a jet with very high granularity based on the Particle Flow Algorithm (PFA) [1–3], while the second aiming at a homogeneous and integrated solution based on the dual-readout concept [4–9]. PFA is the current baseline which is fully integrated in the full CEPC detector simulation.

The basic idea of PFA is to make full use of detector subsystems to determine the energy (momentum) of each particle in a jet. In a typical jet, about 65% of its energy is carried by charged particles, about 25% by photons, and about 10% by neutral hadrons. The charged particles with relative low momentum in a jet can be precisely measured by a Silicon and TPC tracker, and their tracks can be matched to their energy deposits in PFA calorimeters with high granularity. The energy of photons can be precisely measured by crystal ECAL, typically achieving a resolution of $\sim 3\%/\sqrt{E}$. For jets, only about 10% of the energy is carried by neutral hadrons, which are characterized by an intrinsically worse energy resolution of $\sim 60\%/\sqrt{E}$ to be measured by HCAL. An essential prerequisite for realization of this idea is to distinguish among energy deposits of individual particles from a jet in the calorimeter and to minimize the energy confusion among particles. To achieve this objective, high spatial granularity becomes essential. PFA calorimeters consequently employ fine segmentation in three dimensions, with compact and spatially separated particle showers. This design enables precise reconstruction and identification of individual particle showers within jets. In order to achieve the excellent jet energy resolution, extensive studies have been carried out within the CALICE collaboration [10] and within the world-wide Detector R&D (DRD) [11, 12] efforts for future colliders.

For HCAL R&D with high granularity, several technological prototypes have been developed within the CALICE collaboration. The (semi)-digital hadronic calorimeter (SDHCAL) based on glass Resistive Plate Chambers (RPC) [13–17] and the analog hadronic calorimeter using plastic scintillator tiles with SiPM readout (PS-HCAL) [18–21] represent

two prominent approaches. Additionally, the collaboration has explored Micro-Pattern Gaseous Detector (MPGD)-based solutions, including resistive Micromegas and Resistive Plate WELL (RPWELL) technologies [22], as well as digital HCAL (DHCAL) variants. Based on test beam data collected at CERN, the typical energy resolution for single hadrons is about $\sim 60\%/\sqrt{E}$.

The HCAL resolution is one of the main limiting factors in the boson mass resolution with hadronic final states. This motivated us to make tremendous efforts to improve the energy resolution beyond the current technologies discussed above. Building on the experience gained from PS-HCAL, we are now exploring a new approach using high-density glass scintillators as active material. Several types of novel glass scintillators have been developed, featuring high density ($\sim 6 \text{ g/cm}^3$) and light yield (1000 \sim 2000 ph/MeV) with decay time of 100 \sim 1000 ns.

This Glass Scintillator HCAL (GS-HCAL) concept offers significant improvements in energy sampling fraction compared to previous prototypes. While the PS-HCAL achieved about 2% sampling ratio, the use of high-density and thicker glass scintillator increases this to about 30%, promising substantially better energy resolution. Monte Carlo simulation shows that single hadron energy resolution of GS-HCAL can reach $\sim 30\%/\sqrt{E}$. Novel active material, optimal PFA calorimetry design can maximize the overall performance of the jet energy measurement, hence to achieve required jet energy resolution and to fulfill the CEPC physics requirement.

The PFA-based GS-HCAL is adopted as baseline hadronic calorimeter which will result in superior performance. Detail design and performance study of GS-HCAL will be described in this chapter.

1.2 Design

1.2.1 Overall design

The GS-HCAL is a highly segmented calorimeter designed for PFA, consisting of a barrel and two endcaps to ensure full geometric coverage, as shown in Figure 1.2. The detector features 48 layers with a total thickness of 6 nuclear interaction lengths (λ_I), providing fine longitudinal segmentation for precise shower reconstruction. Alternating layers of glass scintillator cells and steel absorber plates achieve fine granularity and sufficient material density to contain hadronic showers, with the active layers segmented into $40 \times 40 \text{ mm}^2$ cells. The barrel forms a cylinder with 16 trapezoidal sectors, while each endcap is similarly divided into 16 sectors arranged in a disk shape. The overall diameter of the barrel measures about 6.9 meters, and its length along the beam axis reaches 6.5 meters.

With approximately 5.22 million cells in total, the GS-HCAL achieves excellent granularity for shower imaging. The active medium consists of glass scintillator cells coupled with silicon photomultipliers (SiPMs) for signal readout, while steel plates serve as the absorber material. The barrel alone weighs about 955 tons, while each endcap weighs around 367 tons, reflecting the robust structure required for mechanical stability and efficient particle detection.

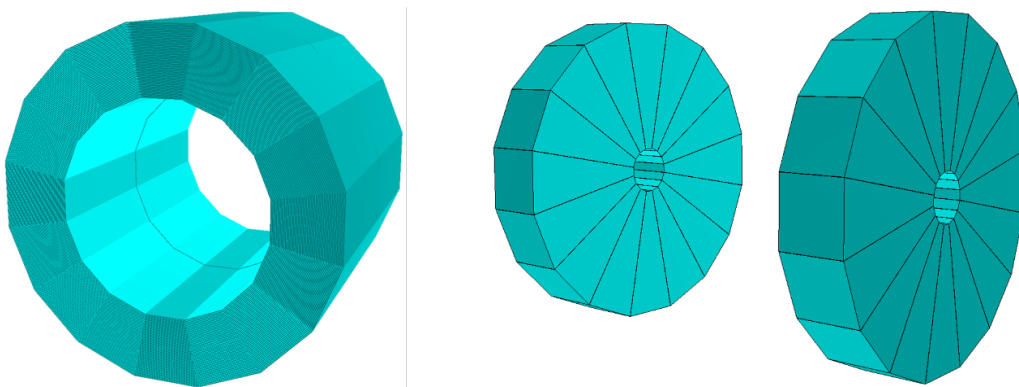


Figure 1.2: Illustration of the GS-HCAL geometry, composed of a barrel and two endcaps. The barrel consists of 16 trapezoidal modules forming an exadecagonal cylinder. Each endcap features 16 trapezoidal modules arranged in a disk shape.

1.2.2 Single layer structure

A single-layer design of the GS-HCAL is illustrated in Figure 1.3. The GS-HCAL consists of alternating layers of glass scintillator cells as the active medium and steel plates as the absorber material. This configuration provides high calorimeter density while maintaining fine segmentation for precise shower imaging.

The total thickness of an individual GS-HCAL layer is 27.2 mm. The top of the layer features a 2 mm-thick upper cover. Below this lies the 10.2 mm-thick glass scintillator active layer with a cell size of $40 \times 40 \text{ mm}^2$ as shown in Figure 1.4, which produces scintillation light when traversed by particles. This is followed by a 3.2 mm layer containing printed circuit board (PCB) and ASIC chips that handle signal processing and readout. A 2 mm-thick bottom cover provides structural support beneath the PCB. The steel absorber forms the base of the structure with a thickness of 9.8 mm. The cooling pipes of $6 \times 6 \text{ mm}^2$ cross-section are embedded in the absorber.

Silicon photomultipliers (SiPMs) are mounted on a PCB that spans multiple glass scintillator cells, with one SiPM positioned at the center of each glass scintillator cell. The material contributions are $0.0805 \lambda_I$, $0.0425 \lambda_I$, and $0.0024 \lambda_I$ for the steel absorber, glass scintillator, and PCB, respectively. The calorimeter's sampling fraction is approximately 31%.

This design optimizes the balance between material interaction length and scintillation efficiency, enabling effective particle detection within a compact cell structure.

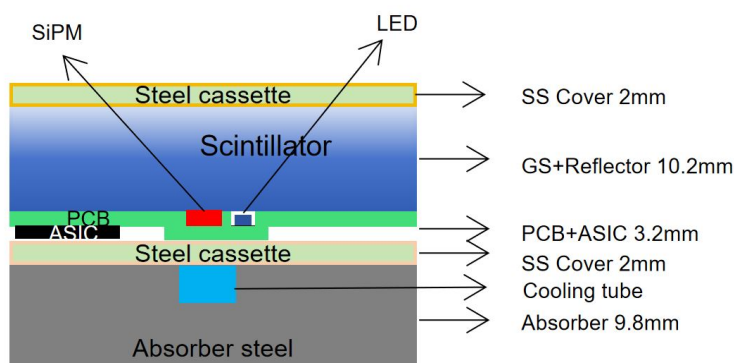


Figure 1.3: Single layer structure of GS-HCAL.

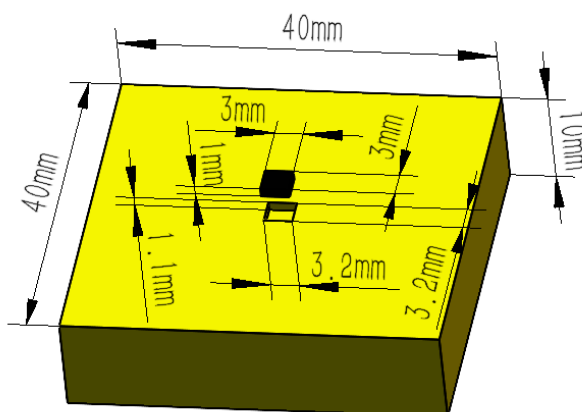


Figure 1.4: Structure of one cell (length unit is mm).

1.2.3 Barrel

The barrel section is divided into 16 trapezoidal sectors, providing a precise and symmetric segmentation, as shown in Figure 1.5. The inner and outer radii of the barrel measure 2140 mm and 3455 mm, respectively, while the length

of the barrel along the beam direction extends to 6460 mm. The trapezoidal shape sector is characterized by a front width of 851.34 mm, corresponding to the narrower side facing the interaction point, and a back width of 1367.56 mm, corresponding to the wider side facing outward. The total thickness of the barrel sector is 1315 mm, ?? verify this number, corresponding to 6 nuclear interaction lengths (λ_I). The longitudinal segmentation is set to 48 layers as needed for PFA. Therefore, the sector gradually expands in width from the front face to the back face while maintaining a uniform height. The weight of the barrel is 955 tons.

Each layer of a barrel sector consists of steel absorber material with active detection elements described in Section 1.2.2. The steel absorber plate serving as the base, upon which 30 or 40 detection boxes are precisely arranged. Each box contains a complete detection unit comprising cover plates, PCB, ASIC chips, etc., as mentioned already. These boxes contain all active components, packaged into modular units for efficient assembly and maintenance, as shown in Figure 1.6. The trapezoidal sector geometry requires adaptive box arrangements across its 48 layers. As each layer's width decreases from the outer to inner, three box widths (320 mm, 280 mm, and 240 mm) are combinatorially deployed to maintain full coverage. The outermost layers employ four 320 mm boxes, while progressively inward layers use mixed combinations (e.g., three 320 mm plus one 280 mm box) to accommodate the narrowing profile. The innermost layers transition to three 280 mm boxes, ensuring optimal surface coverage throughout the sector's radial gradient with minimized gaps. This scheme preserves the $40 \times 40 \text{ mm}^2$ cell granularity while accommodating the sector's geometric constraints.

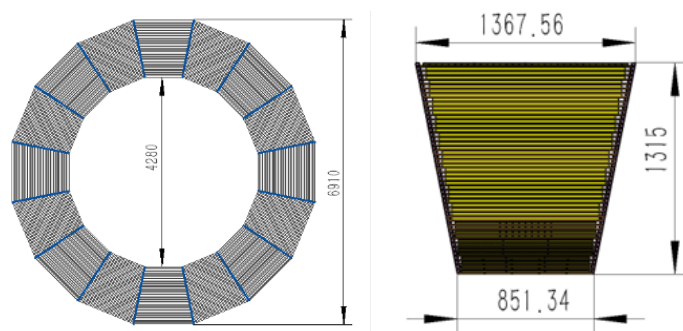


Figure 1.5: Dimensions of the GS-HCAL barrel. (a) HCAL Barrel cross-sectional view showing 16 trapezoidal sectors arranged in a ring with an inner diameter of 4280 mm and an outer diameter of 6910 mm, ?? verify this number. (b) Side view of a single trapezoidal module along the beam direction, with a front width of 851.34 mm, a back width of 1367.56 mm, and a height (depth) of 1315 mm, ?? verify this number.

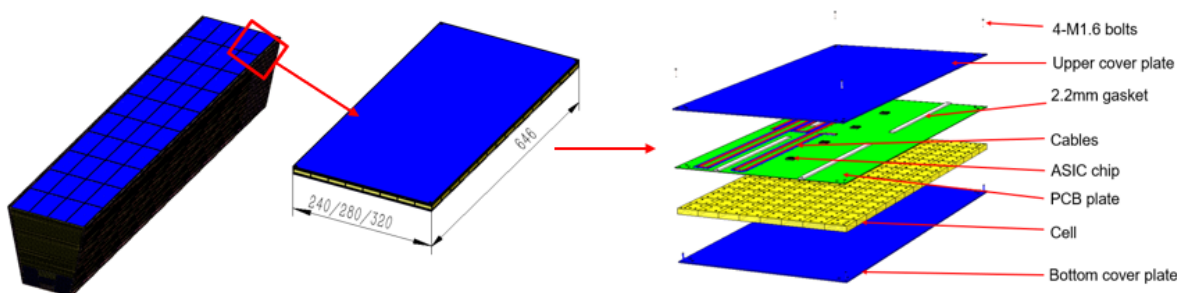


Figure 1.6: Illustration of the GS-HCAL sector structure. The left figure shows a full barrel sector composed of 48 layers; the middle one illustrates the dimensions of an individual box with varying widths (240/280/320 mm) and a fixed length of 646 mm; the right figure presents the internal structure of a single box, including the cover plates, glass scintillator cells, PCB with ASIC chips, cables, and cooling gasket.

Taking the 48th layer of one sector as an example, it consists of four 320 mm wide boxes arranged side-by-side, each with a uniform length of 646 mm to cover the full sector width at this layer position, while 10 boxes to cover the full barrel length along the beam direction, as shown in Figure 1.7. Each 320 mm box contains eight glass scintillator cells ($40 \times 40 \text{ mm}^2$) along its width ($320/40 = 8$ cells) and sixteen cells along its length ($646/40 \sim 16$ cells), totaling 128 cells in this box. Across the entire layer, this configuration provides 5120 cells ($4 \times 10 \times 128$ cells). The 40 boxes are precisely positioned on the steel absorber plate. Each box is first aligned using registration pins, then secured with four bolts through

the corner mounting holes as shown in Figure 1.8 illustrating how the box corner is connected. Each corner features three holes: one for box assembly, one for precision alignment pins, and one for final bolts that structurally connect adjacent absorber layers. Adjacent boxes maintain a 2 mm gap for thermal expansion while their cover plates interlock to ensure mechanical stability across the full sector width.

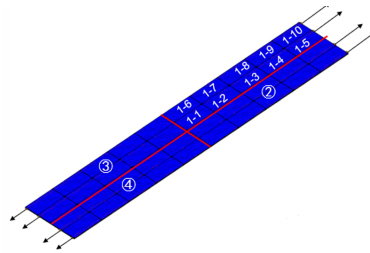


Figure 1.7: Illustration of the arrangement of 40 boxes in the outer most (48th) layer.

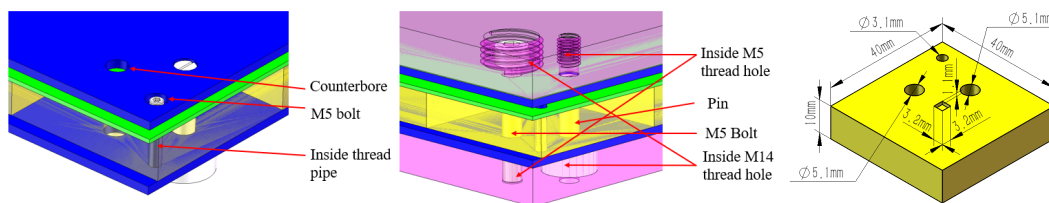


Figure 1.8: [redraw] Structure of box corner. Left plot shows the box corner alone, middle plot gives the structure attached to absorber, and the right side plot shows the glass scintillator cell used in the corner.

The cables are housed within each box between the upper cover plate and PCB plate, as shown in Figure 1.6. Each box contains five 2 mm-diameter cables of uniform length within the box, with five lengths (0.40 m, 1.05 m, 1.70 m, 2.35 m, 2.90 m) distributed across different boxes in the layer. Following box installation, the cables are carefully bent and routed to end-mounted administration boards (Figure 1.9). Each layer features either 2×4 or 2×3 administration boards (each measuring 20×60 mm), with each board receiving inputs from 25 cables and providing two output cables plus one fiber optic connection. The 2 mm-diameter cables follow separate front and back routing paths, illustrated in Figure 1.10.

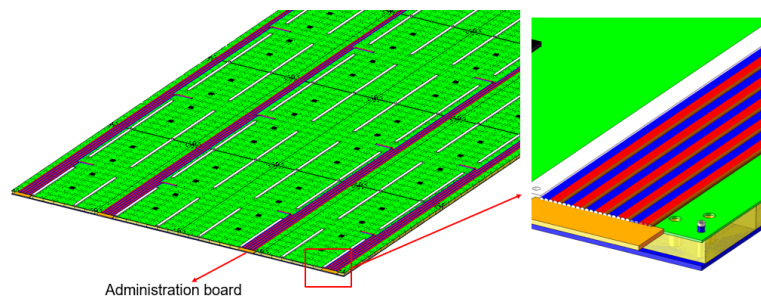


Figure 1.9: PCB board structure with cable arrangement.

This layered architecture repeats 48 times along the depth of the sector, with each new layer positioned directly atop the previous one. The steel absorber plates (9.8 mm thick) provide both structural support and the necessary interaction length, while the interspersed boxes maintain precise alignment through alignment pins between layers.

Between the upper and lower absorber layers, two trapezoidal support beams are integrated to maintain stability. Detailed illustrations of this arrangement can be seen in Figure 1.11. Each sector assembly is completed layer by layer, where edge sealings and bolts are used to ensure robust mechanical connectivity and structural integrity throughout the system.

A water cooling system is specifically designed to manage thermal loads mostly from the ASIC chips. A total heat load of 76.8 W per layer (5120 channels \times 15 mW/ch) generated by the front-end electronics. As shown in Figure 1.12, each of the 48 layers in a sector incorporates 4 water cooling pipes embedded within the steel absorber plates, positioned in

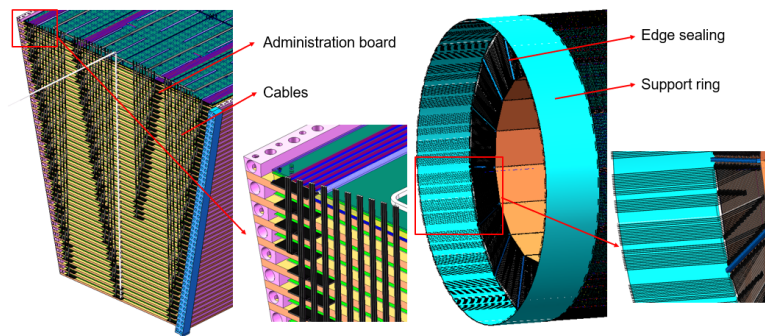


Figure 1.10: The front and back cable routing scheme.

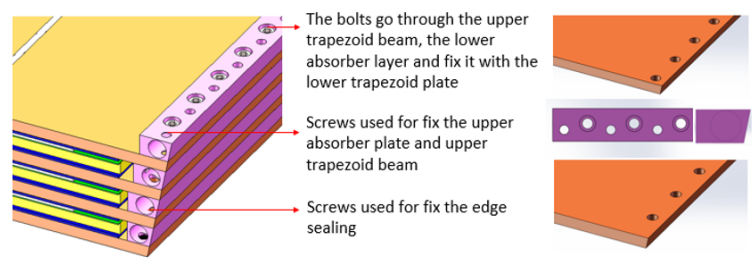


Figure 1.11: Connection between two absorber layers and adjacent sectors.

close proximity to the PCB-mounted ASIC chips. The system is organized hierarchically with shared coolant distribution: every eight consecutive layers are grouped together, sharing common input and output manifolds. This configuration results in six independent cooling loops per sector (48 layers / 8 layers per group), each with dedicated supply and return piping. The localized four-pipe arrangement per layer ensures efficient heat extraction from the ASICs, while the grouped manifold system simplifies the overall cooling infrastructure.

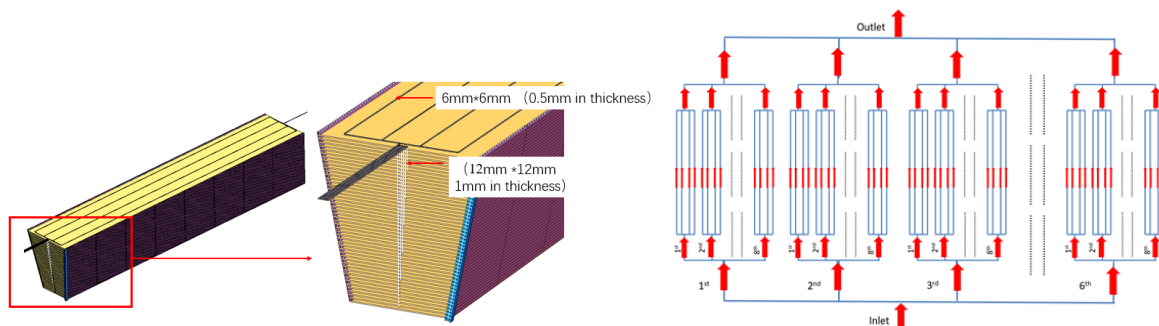


Figure 1.12: Cooling pipe structure for each sector (left) and the water circulating routes (right).

For barrel, there are totally 200800 cells for each sector, so the amount of the cell for barrel is 3212800. The number of boxes for each sector is 1740, for the whole barrel HCAL, the amount is 27840. Table 1.1 lists the weight data, with a total weight of the barrel about 955 tons.

1.2.4 Endcap

The endcap section complements the barrel to provide full geometric coverage at both ends along the beam direction, as shown in Figure 1.13. The dimension and structure match with the barrel design as 16 sectors, 450 mm inner radius and 3455 mm outer radius. The thickness of sector also keeps consistent with barrel as 1360 mm, ?? verify this number, which consists of 48 layers. The trapezoidal shape shown in the figure corresponds to one sector of the GS-HCAL endcap. It has a top width of 1307 mm and a total height of 2862 mm measured along the radial direction from the beam axis. The sector has a wider outer edge toward a narrower inner tip. It is divided into six boxes along the radial direction. The top four boxes are arranged symmetrically in two pairs, and the bottom two boxes are single. The endcap shares the

Table 1.1: Weight data of different components of barrel HCAL.

Items	Weight/wedge (kg)	Weight/barrel (T)
Cover plate	10287	164.6
PCB plate	390	6.2
GS scintillator	19277	308.4
Absorber layer	27515	440.2
Support structure	1883	30.1
Auxiliaries	350	5.6
Total	59702	955.2

same single layer structure as that of the barrel, as detailed in Section 1.2.2. This segmentation supports both mechanical integration and longitudinal sampling for hadronic shower reconstruction. Each endcap weighs 362 tons, reflecting its substantial construction.

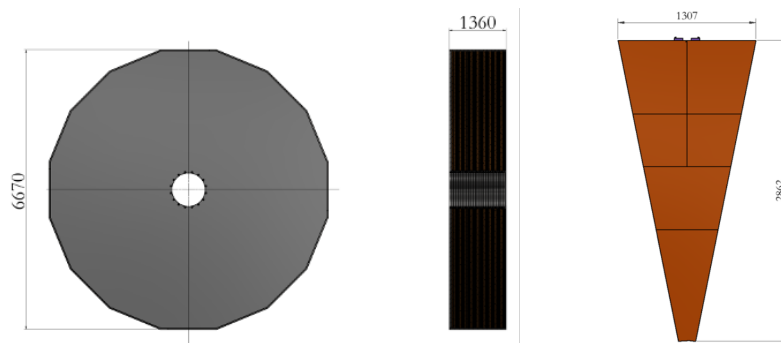


Figure 1.13: Dimensions of the GS-HCAL endcaps. (a) Front view of the endcap along the beam axis, showing the full diameter of 6670 mm, ?? verify this number, (b) Side view revealing the endcap thickness of 1360 mm, ?? verify this number; (c) Detailed view of a single sector - the complete endcap consists of 16 such identical sectors.

Figure 1.14 and 1.15 illustrates the assembly procedure for the endcap, which follows a horizontal installation scheme. The construction begins with 1405 individual detector cells assembled into a single sector layer, with 16 of these sector layers combined to form one complete disc-shaped layer. A total of 48 such layers are sequentially stacked to complete the module. The assembly process starts with mounting a 50 mm-thick outer structural plate (non-absorbing) to provide rigidity and serve as the installation reference. Active layers and steel absorber plates are then alternately installed horizontally. Specialized tools carefully rotate the assembled components into their final vertical orientation, with particular attention to preventing excessive pressure on the crystals throughout the process to ensure their integrity.

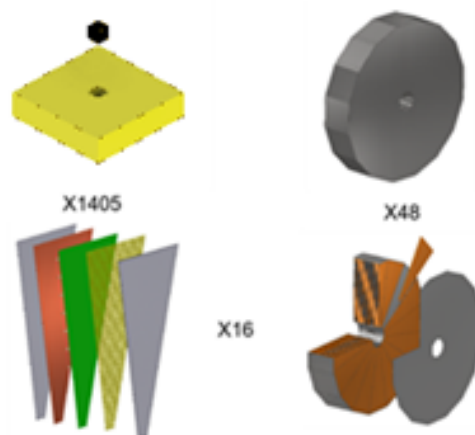


Figure 1.14: Formation of the endcap HCAL model

[fixme] Figure 1.16 shows the endcap water cooling system. Each detector layer has 16 separate cooling regions.

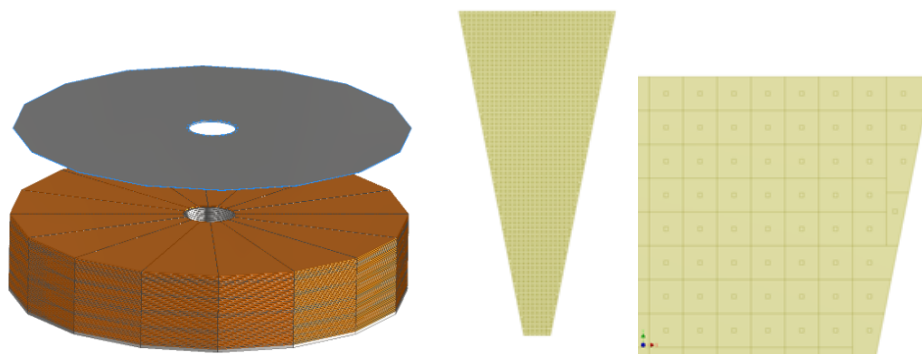


Figure 1.15: Horizontal installation scheme and gapless glass tile arrangement.

Each region contains one dedicated cooling water channel. This creates 16 directional cooling paths per layer. When all 48 layers are assembled, matching channels connect vertically, forming parallel water circuits through the stack. The system uses a 4×4 square pattern of pipes, with each pipe having a 12 mm inner diameter. In total, there are 48 parallel cooling pipes in the complete endcap structure.

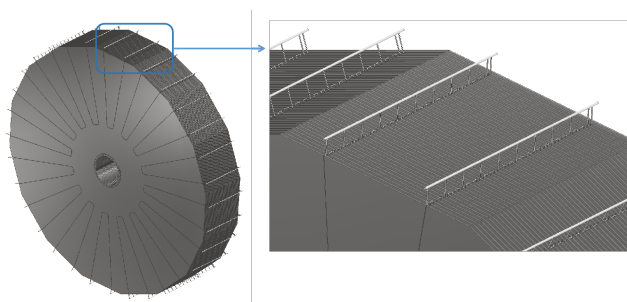


Figure 1.16: Cooling pipe structure for GS-HCAL endcap.

1.2.5 Connection to other detectors

The GS-HCAL barrel interfaces with two key detector components through specialized connection systems. Two auxiliary rings provide the mechanical linkage to the Yoke, implemented via edge-sealing technology as illustrated in Figure 1.17. Similarly, the barrel-to-ECAL connection employs edge-sealing between components, with the detailed interface geometry shown in Figure 1.18. Both connection systems maintain precise alignment while accommodating thermal and mechanical stresses.

[fixme, how about Endcap?]

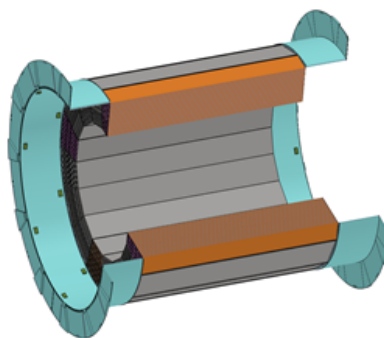


Figure 1.17: [fixme, how exactly?] Connection structure between barrel HCAL and barrel Yoke.

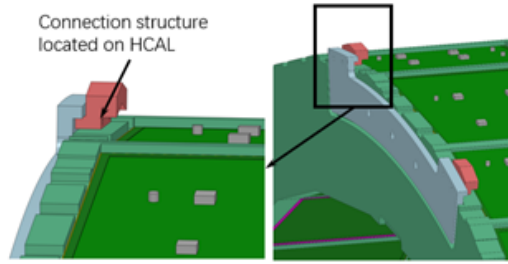


Figure 1.18: [fixme, how exactly?] Connection structure between barrel HCAL and barrel ECAL.

1.2.6 Summary

Table 1.2 gives the numbers of cells, boxes, layers, and sectors for the GS-HCAL barrel and endcap. The barrel consists of 16 sectors, each composed of 48 layers, totaling 768 layers, with 27,840 boxes and 3,212,800 cells. Each endcap is built with 16 sectors and 48 layers, corresponding to 3,072 boxes and 1,006,080 cells per endcap. Since there are two endcaps and one barrel, the total number of cells are about 5.22 millions.

Table 1.2: Numbers of cells, boxes, layers, and sectors for the GS-HCAL barrel and endcap.

Part	Cell	Box	Layer	Sectors
Barrel	3,212,800	27,840	48×16	16
Endcap (2 sides)	$1,006,080 \times 2$	$3,072 \times 2$	$48 \times 16 \times 2$	16×2

1.3 Key technologies and major challenges

The CEPC GS-HCAL, leverages several advanced technologies and strategies to address critical challenges posed by its stringent physics requirements. These technologies encompass enhancing glass scintillation properties, optimizing photon detection efficiency, addressing glass weight and mechanical integration, managing detector cost, and mitigating SiPM noise.

One critical technology aspect is the optimization of glass scintillator properties, particularly regarding the light yield and attenuation length. The GS-HCAL employs high-density glass scintillators (approximately 6 g/cm^3) with moderate intrinsic light yields around 1000-2000 photons per MeV. Although glass scintillators intrinsically exhibit lower photon yields compared to crystals, careful optimization, including surface polishing and reflective coatings, can achieve substantial effective light yields (80–100 p.e./MIP). [TODO: need to say attenuation length is now 6.2 cm, it is no more a problem.] The currently limited attenuation length of 2.3 cm poses a challenge for light collection uniformity, which can be mitigated by increasing the attenuation length to around 6 cm, embedding wavelength-shifting fibers (WLS), or employing multiple SiPM readouts per scintillator tile.

The significant weight of glass scintillator materials introduces a major mechanical engineering challenge. Each endcap of the GS-HCAL alone weighs 362 tons, while the barrel weighs 955 tons, mandating robust, yet precisely aligned mechanical structures. To manage the considerable loads, a modular design approach featuring rigid frames and carefully engineered cassette-style modules has to be adopted, facilitating installation, maintenance, and ensuring mechanical stability and alignment precision throughout the detector's lifetime.

To validate and refine the proposed design solutions, extensive prototyping and testing of the GS-HCAL have to be undertaken. The GS-HCAL prototype should include alternating layers of high-density glass scintillator and steel absorber, read out by advanced SiPMs. Test beam studies have to be performed to confirm the feasibility of achieving the targeted energy resolution around $30\%/\sqrt{E}$, validating the design's potential in meeting stringent CEPC physics requirements.

SiPMs, critical components for photon detection, have been selected due to their compactness, insensitivity to magnetic fields, and high Photon Detection Efficiency (PDE), which can exceed 50% at the relevant wavelengths (420–460 nm). Achieving high PDE is crucial for compensating the moderate intrinsic photon yield from the glass scintillators. Despite these advantages, SiPMs present challenges such as dark noise, with typical rates of tens to hundreds of kHz per

mm². To address this, further work is required to implement effective strategies such as operational cooling, development of advanced electronics for noise filtering, and design of sophisticated data acquisition algorithms, in order to enable suppression of dark noise and ensure high detector sensitivity.

Cost considerations significantly influence the technological strategies adopted for the GS-HCAL. With millions of readout channels envisioned, the cost-per-channel of SiPMs and scintillator production will substantially impact overall project economics. To address this, collaborative procurement strategies and industry partnerships must be further developed to manage SiPM costs, and advancements in scalable manufacturing processes for glass scintillators need to be pursued to reduce costs, with the goal of making glass scintillators economically competitive compared to traditional plastic alternatives.

Addressing mechanical challenges, the structural design must ensure mechanical rigidity, precision alignment, and ease of assembly and maintenance. Innovations such as modular cassette-based designs are under development to enable manageable assembly and efficient replacement or servicing, which will be critical for maintaining detector performance over extended operational periods.

In summary, the GS-HCAL for CEPC aims to address multiple technological challenges through focused R&D efforts in scintillator optimization, photon detection technologies, cost-effective production methods, noise reduction techniques, and advanced mechanical design solutions. These ongoing strategic developments are essential to enable the realization of a highly granular, cost-effective, mechanically robust, and high-performance calorimeter required to meet CEPC's ambitious physics goals.

1.4 Past R&D to demonstrate technologies and prototypes

The pursuit of high-performance hadron calorimetry has long been driven by the need to balance cost, radiation hardness, and energy resolution. Among the various scintillator materials explored, glass scintillators have emerged as a compelling candidate, offering a unique combination of high density, moderate light yield, and scalability—qualities essential for next-generation collider experiments. The evolution of glass scintillators in calorimetry reflects a series of iterative advances, from early exploratory designs to modern granular systems enabled by breakthroughs in photodetection and signal reconstruction. This section reviews the key milestones in glass-scintillator R&D, with particular emphasis on recent developments that have transformed their feasibility for large-scale hadronic calorimeters (HCALs).

The conceptual foundation for glass scintillators in calorimetry dates to the 1980s, spurred by the Crystal Clear Collaboration [23] at CERN, which pioneered investigations into high-Z glass matrices for electromagnetic calorimeters (ECALs). Among the earliest prototypes, the HED-1 glass scintillator calorimeter, developed by TU Dortmund University in 1988, demonstrated the material's potential despite limitations in radiation length and light output. Comprising modular arrays of $8 \times 8 \times 66$ cm³ blocks, HED-1 highlighted the trade-offs inherent in early glass scintillators: while their radiation hardness and short decay times were advantageous for high-rate environments like B-factories, their inferior light yield necessitated the use of photomultiplier tubes (PMTs) to compensate. Subsequent efforts, such as CERN's exploration of cerium-doped heavy metal fluoride glasses (HFG:Ce), further underscored these challenges. Although HFG:Ce achieved satisfactory optical quality in large volumes (e.g., $15 \times 3 \times 3$ cm³), its susceptibility to radiation damage rendered it impractical for high-luminosity experiments. These early endeavors revealed a critical gap—the need for a material that could simultaneously deliver high density, radiation resistance, and efficient light transmission—a gap that remained unresolved for decades due to technological constraints.

A persistent limitation of traditional glass scintillators was their excessive self-absorption, which severely attenuated light output in long-bar geometries. This drawback stifled numerous proposals for scintillating glass-based calorimeters, as the resulting light yield fell short of the requirements for precise energy reconstruction. However, two transformative advancements in the 2010s redefined the feasibility of glass scintillators: the maturation of silicon photomultipliers (SiPMs) and the adoption of particle flow algorithms (PFA). The mass production of SiPMs drastically reduced the cost of high-efficiency photodetection, enabling the use of granular scintillator blocks where light collection no longer depended on long attenuation lengths. Concurrently, PFA-based calorimetry eliminated the need for longitudinal light transmission by leveraging fine-grained spatial segmentation and topological clustering, shifting the focus to compact, optically isolated

cells. These innovations relaxed the stringent light-yield requirements for glass scintillators, provided they could achieve a minimum threshold of 1000 ph/MeV and couple with SiPMs exhibiting $\geq 40\%$ photon detection efficiency. This paradigm shift rendered previously impractical designs viable, reigniting interest in glass scintillators as a cost-effective alternative to crystals and plastics.

Recent developments (post-2020) have focused on optimizing the density-light yield balance while ensuring scalability for large-scale detectors. A landmark initiative in this direction is the Glass Scintillator Hadron Calorimeter (GS-HCAL) project, proposed in 2021 by a collaboration led by the Institute of High Energy Physics (IHEP) and involving multiple Chinese institutes and industrial partners, as part of the CEPC detector R&D program. The GS-HCAL design leverages granular glass scintillator tiles with densities of approximately 6 g/cm^3 , read out by SiPM arrays to achieve high-precision energy sampling. Modern glass formulations developed for this project now achieve light yields of 1000–2500 ph/MeV despite inherent self-absorption, meeting the stringent resolution requirements for jet energy reconstruction in particle-flow calorimetry. Advances in activator doping (e.g., Ce^{3+}) and matrix composition (e.g., fluorides) have produced glasses with decay times $\mathcal{O}(500)$ ns, such as Ce^{3+} -doped Gadolinium Fluoro-Oxide (GFO) with light yield of about 1700 ph/MeV. These material advancements are complemented by progress in mass production techniques, such as continuous melting and precision molding, which are critical for achieving cost targets competitive at the scale required for the CEPC.

The current phase of GS-HCAL R&D is marked by rapid progress toward bridging the gap between prototype validation and industrial production. Collaborative efforts, including the worldwide DRD collaborations and the GS collaboration of Chinese universities, research institutes, and industry partners, are systematically addressing key challenges such as inter-tile uniformity, SiPM integration, and system-level radiation tolerance. Recent advancements have further accelerated the project's readiness, with improvements in glass quality, SiPM performance, and modular assembly techniques. The successful testing of $4 \times 4 \times 1 \text{ cm}^3$ GFO GS tiles in 2023 has been followed by larger-scale validations, paving the way for a full-size prototype R&D. These developments position GS-HCAL as a transformative solution for the CEPC's calorimetry system, offering a viable path to hadronic energy resolution of $\sigma/E \sim 30\%/\sqrt{E}$, a benchmark previously unattainable with conventional materials. The following subsections detail the technical milestones and experimental results underpinning this progress, from material synthesis to beam tests and simulation-based optimization.

[\[add references\]](#)

1.4.1 Glass scintillator

The development of high-performance scintillation glass is fundamental to the success of the GS-HCAL project. The gadolinium-based fluoride oxide (GFO) glass has been selected as the baseline material due to its optimal balance between performance characteristics and manufacturability for large-scale production. As detailed in Table 1.3, GFO glass achieves a density of 6.0 g/cm^3 with favorable radiation length (1.59 cm) and nuclear interaction length (24.2 cm), making it particularly suitable for hadronic shower measurements. While BGO crystals show superior absolute performance in some parameters, GFO's competitive light yield (1739 ph/MeV), fast decay components (57.6 ns), and lower production temperature (1250°C) present significant advantages for CEPC deployment.

The glass composition features Ce^{3+} as the luminescent center, chosen for its strong emission, fast decay, and efficient energy transfer from Gd^{3+} modifiers [24]. The borosilicate matrix ($\text{B}_2\text{O}_3\text{-SiO}_2$) provides excellent thermal and optical properties, with Al_2O_3 additives enhancing chemical stability. Gadolinium serves as the optimal heavy element modifier, offering high density while maintaining low radioactivity and cost-effectiveness compared to La or Lu alternatives.

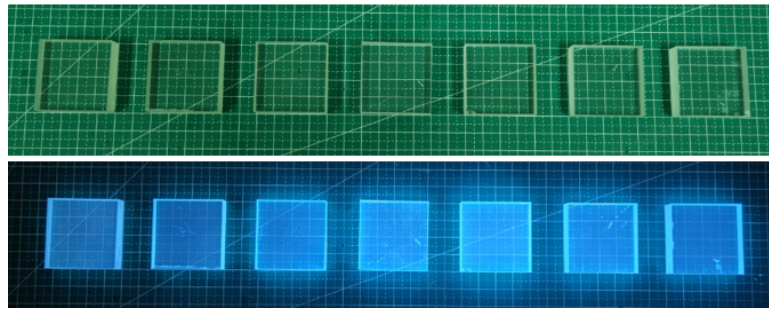
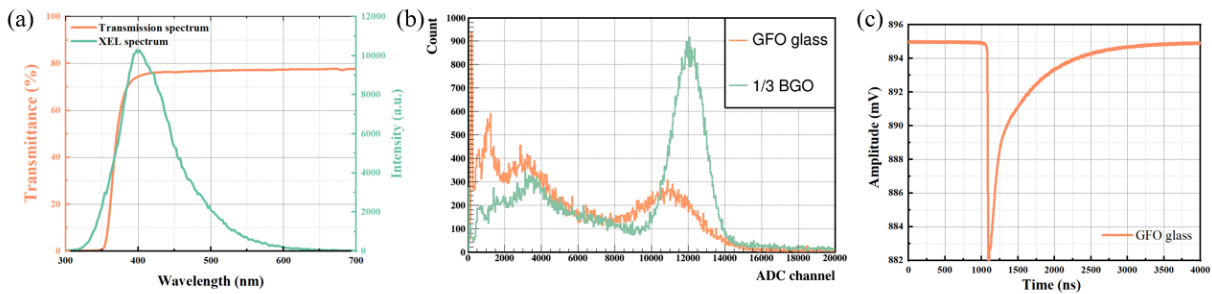
1.4.1.1 Light yield

Figure 1.19 shows the photograph of GFO glasses with $40 \times 40 \times 10 \text{ mm}^3$ under natural and ultraviolet light. Extensive γ -ray testing has demonstrated that the light yield of GFO glasses can consistently exceed 1000 ph/MeV. When measured with an XP2020 PMT, the detected photo-electron number reaches 1/3 that of BGO crystals with identical dimensions, as shown in Figure 1.20(b). Figure 1.20(c) presents the scintillation decay profile of GFO glass under γ -ray excitation. While maintaining a light yield of 1000 ph/MeV, the decay time of the slow component can be controlled to below 500 ns. Although achieving faster decay time remains challenging, the large-scale GFO glass successfully maintains an optimal

Table 1.3: Key parameters of the glass scintillator (GFO) with a size of $5 \times 5 \times 5 \text{ mm}^3$, compared with the Bismuth Germanate (BGO) [25] and DSB glass [26].

Key parameters	GFO glass	BGO	DSB Glass
Density (g/cm^3)	6.0	7.13	4.2
Melting point ($^\circ\text{C}$)	1250	1050	1550
Radiation Length (cm)	1.59	1.12	2.62
Molière radius (cm)	2.49	2.23	3.33
Nuclear interaction length (cm)	24.2	22.7	31.8
Z_{eff}	56.6	71.5	49.7
dE/dX (MeV/cm)	8.0	8.99	5.9
Emission peak (nm)	400	480	430
Refractive index	1.74	2.15	
Light yield (ph/MeV)	~ 1500	7500	2500
Energy resolution (% @662keV)	~ 23	9.5	
Scintillation decay time (ns)	~ 60 and 500	60, 300	90, 400

balance between density, light yield, and scintillation decay characteristics.

**Figure 1.19:** GFO glass tiles of the size $40 \times 40 \times 10 \text{ mm}^3$ under natural light and ultraviolet light.**Figure 1.20:** (a) Transmission and XEL spectra of large GFO glass, (b) Energy spectra of GFO glass scintillators and BGO crystal with same dimension. (c) Scintillation decay curves of GFO glass

However, as illustrated in Figure 1.20(a), these glasses still exhibit strong self-absorption in the ultraviolet spectral region. Additionally, as the glass thickness increases, its transmittance in the visible spectrum decreases from approximately 80% to around 75%. The measurable light output of GFO glass became a critical factor for HCAL applications.

[todo: add a table to summarize the light yields of the $4 \times 4 \times 1 \text{ cm}^3$ size of the GFO glass tile.]

To evaluate the performance of glass scintillator (GS) dedicated beam tests and cosmic ray measurements were conducted, using $40 \times 40 \times 10 \text{ mm}^3$ GS tiles, and read out by SiPMs.

Nine GS tiles were exposed to 5 GeV electron beam at the DESY test facility. The acquisition system was configured with an integral gate of $1 \mu\text{s}$ to capture the scintillation signal, reading out using Hamamatsu S13360-6025PE SiPM.

The resulting photoelectron (p.e.) spectrum showed a most probable value (MPV) of approximately 90–100 pe/MIP. The measured light yield was in the range of 600–700 photons/MeV, consistent with expectations for high-density GS tiles. The setup is illustrated in the left panel of Figure 1.21, with the corresponding P.E. spectrum shown on the right side.

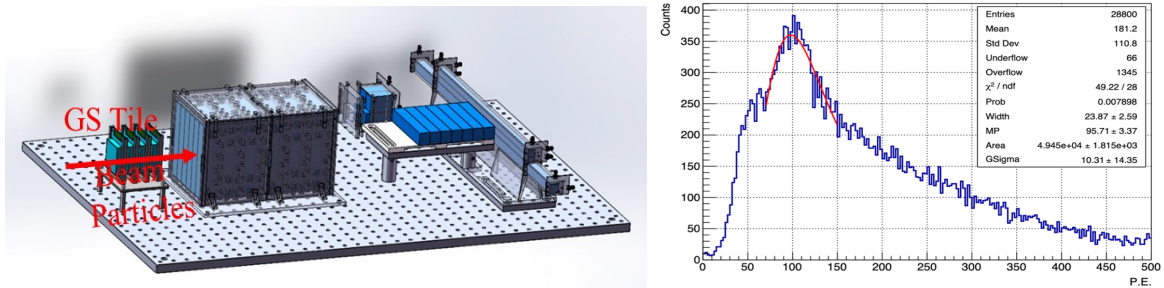


Figure 1.21: DESY electron beam test of the GFO glass tiles in 2023. Left figure shows the experimental setup, right figure shows the measured p.e. distribution.

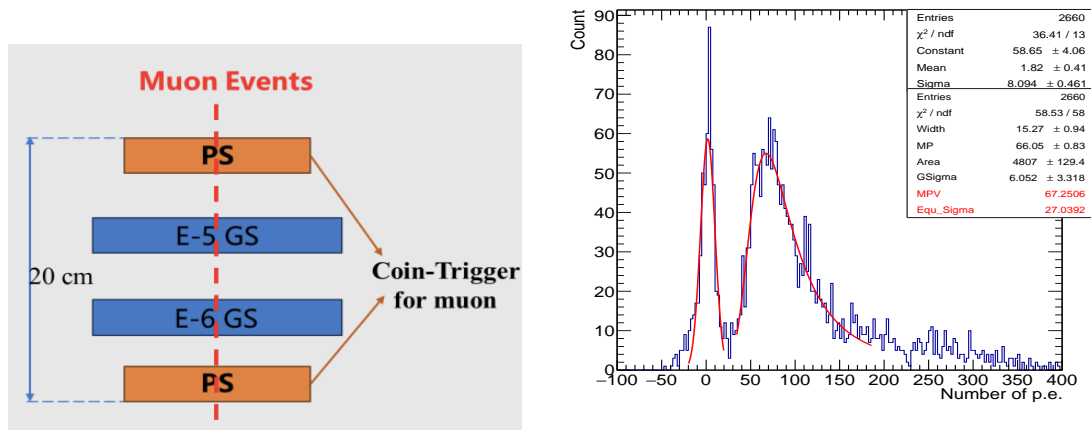


Figure 1.22: IHEP cosmic ray setup performed in 2024 of GFO glass tiles (left), and the measured p.e. distributions for MIPs (right).

To independently validate the MIP response, a second measurement was performed using cosmic muons in a vertical stack configuration at IHEP in 2024. Two plastic scintillator (PS) paddles provided coincidence triggers above and below the GS tiles (labeled E-5 and E-6) to ensure clean muon tracks. This setup is schematically shown in the left panel of Figure 1.22. The readout is using Hamamatsu S13360-6025CS SiPM. A longer integral gate of $4 \mu\text{s}$ was employed to fully collect the slower scintillation components. The measured MIP response for the E-5 tile reached an MPV of approximately 70 pe/MIP, corresponding to an inferred light yield of ~ 750 photons/MeV, which is consistent with the DESY results. [to be checked].

Both measurements confirm the feasibility of using GS tiles for high-granularity HCAL applications. A summary of the results is presented in Table 1.4. These results validate the promising performance of glass scintillator tiles and provide critical input for optimizing the calorimeter design for CEPC.

Table 1.4: Summary of GS tile beam test and cosmic ray measurements.

Test Setup	Integral Gate	Light Yield	MIP Response
DESY Electron Beam	$1 \mu\text{s}$	600–700 ph/MeV	90–100 pe/MIP
IHEP Cosmic Ray (E-5)	$4 \mu\text{s}$	~ 750 ph/MeV	80–90 pe/MIP

1.4.1.2 Light attenuation length

[TODO: Improve the text to say that 3.4 cm is the average for all γ -ray spectrum, but 6.2 cm is the value at 400 nm.]

The attenuation length (L_0) is a critical parameter for evaluating light transmission performance in scintillators. Multiple batches of GFO glass samples with cross-sectional dimensions of $5 \times 5 \text{ mm}^2$ and thicknesses ranging from 1–15 mm were prepared for systematic measurements (Fig. 1.23). The best-performing GFO glass sample currently available achieves an **attenuation length of 6.2 cm at 400 nm**. This value is used as the standard reference in the TDR, and all performance results are based on it.

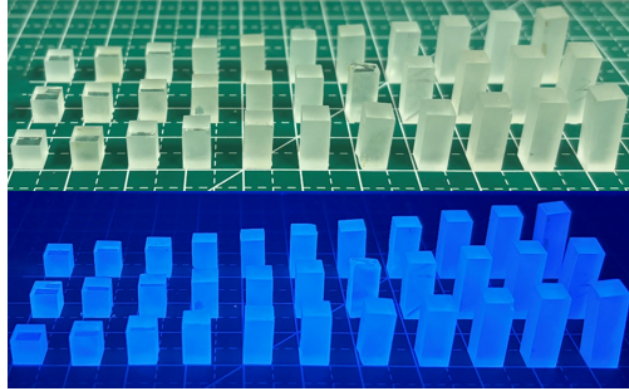


Figure 1.23: GFO glass samples under natural light (top) and ultraviolet light (bottom).

The light attenuation follows the exponential relation:

$$LY = LY_0 \exp\left(-\frac{L}{L_0}\right) \quad (1.1)$$

where LY_0 is the initial photon yield, LY the yield after propagation distance L , and L_0 the characteristic attenuation length. Initial measurements yielded $L_0 = 2.3 \pm 0.01 \text{ cm}$ [27], limited by glass matrix defects and Ce^{3+} self-absorption.

Through process optimization, the GFO light yield increased from 1000 to over 1500 ph/MeV, suggesting corresponding attenuation length improvements. Figure 1.24 illustrates the γ -ray spectral method for determining the light attenuation length. The method involves measuring the ratio of the initial light yield (LY_0) to the light yield after transmission through varying glass thicknesses (LY). By fitting this ratio as a function of thickness, we extract the attenuation length, yielding a value of $L_0 = 2.3 \text{ cm}$ and $L_0 = 3.4 \text{ cm}$ for two batches of glass samples before and after optimization, respectively.

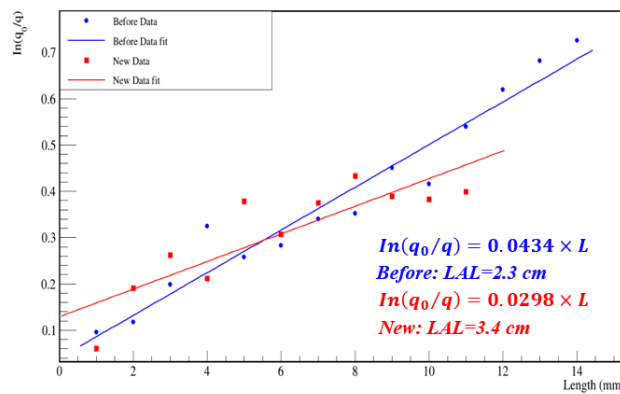


Figure 1.24: Light yield ratio $\ln(LY_0/LY)$ as a function of the thickness of the glass is fitted to extract light attenuation length (LAL).

A more accurate method determines L_0 through thickness-dependent transmittance (T):

$$L_0 = \frac{L_2 - L_1}{\ln(T_{L_1}/T_{L_2})} \quad (1.2)$$

where T_L is the transmittance at thickness L . This method accounts for full-volume light penetration, eliminating position uncertainty. Figure 1.25 shows the improved attenuation length of 6.2 cm at 400 nm (emission peak), with consistent 5.8–6.2 cm performance across the visible spectrum - a 100% improvement over previous samples (3.1 cm at 400 nm). These results confirm that γ -ray methods systematically underestimate L_0 , while verifying GFO's about 6 cm attenuation

length enables efficient light collection.

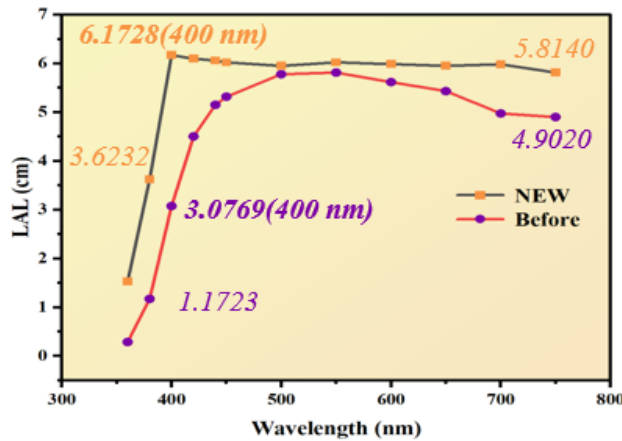


Figure 1.25: Attenuation length spectrum from transmittance measurements (solid line: current GFO, dashed line: previous samples).

1.4.1.3 Radiation resistance

The radiation resistance of glass scintillators is crucial as their performance degrades after irradiation. The GFO glass samples were studied using an 80 MeV proton beam at the Associated Proton Beam Experiment Platform (APEP) [28] across a wide dose range (400 Gy to 4.1×10^4 Gy). Proton flux for this test is 4.86×10^9 (p/cm²/s), and the beam spot size is 50×50 mm². Seven $10 \times 10 \times 10$ mm³ pieces (labeled #1-#7) were used for this test, using different radiation time to obtain corresponding radiation dosage as shown in Table 1.5). Sample #1 kept as an unirradiated reference.

The scintillation properties were characterized through transmission spectra, X-ray excited luminescence (XEL), light output, and decay time measurements (Table 1.5). Unirradiated sample showed 78% transmittance at 400 nm, while transmittance of irradiated samples dropped to 31% with a dose of 800 Gy, and further dropped to 10% for a dose of 8100 Gy, consistent with visible color changes indicating defect formation. The Ce³⁺ emission peak (386 nm in unirradiated samples) shifted slightly to 376-384 nm after irradiation. Figure 1.26 displays the visual changes in samples #1 to #7 under progressively higher radiation doses, with increased dosage correlating to decreased transparency and darker color.

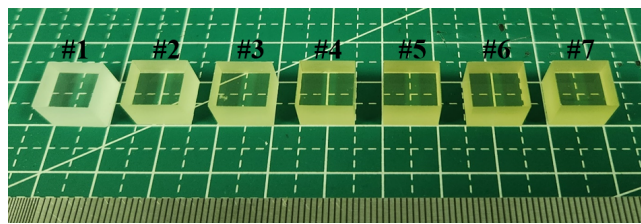


Figure 1.26: The photograph of proton beam irradiated glass samples. From sample #1 to #7, the radiation dosage progressively increases, resulting in darker color with decreased transparency.

Table 1.5: Performance summary of the glass tiles after proton irradiation test.

Sample	Dose (Gy)	Transmittance @ 400nm (%)	XEL (nm)	Light Output (ph/MeV)	Decay Time (τ) (ns)
#1	0	77.9	386	552	87, 985
#2	400	37.4	376	187	89, 980
#3	800	31.3	380	–	–
#4	2000	13.7	384	–	–
#5	4100	10.4	376	–	–
#6	8100	8.3	380	–	–
#7	41000	5.8	376	–	–

In contrast to proton irradiation, gamma irradiation tests evaluate performance degradation at lower doses (10-400 Gy). A ^{60}Co point source (3.656×10^{11} Bq) was used, emitting gamma rays at 1.1732 MeV and 1.3325 MeV as shown in Figure 1.27 (a). The absorbed dose rate follows the inverse square law relative to the source distance. Six $5 \times 5 \times 5$ mm³ glass samples were irradiated simultaneously for 37.5 hours at varying distances (10-63 cm) to achieve different dose rates as shown in Table 1.6. Figure 1.27 (b) and (c) present the experimental setup and slight yellowing for samples with higher radiation dosage.

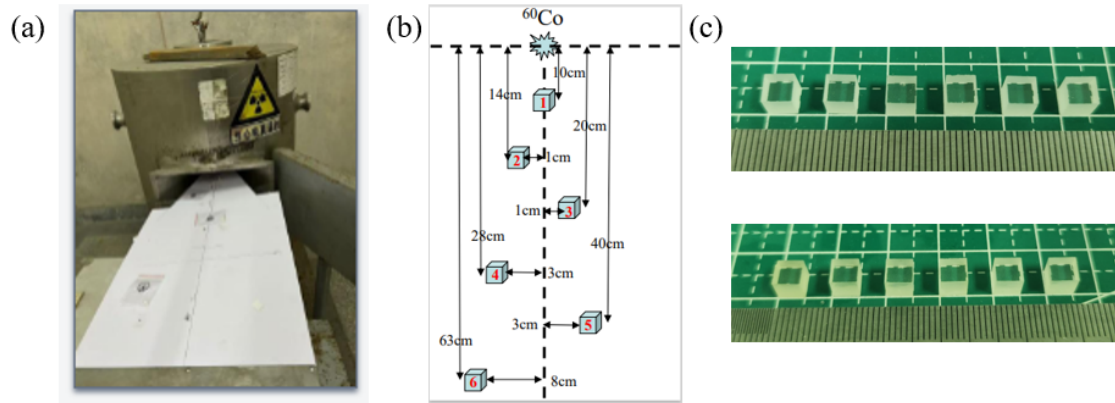


Figure 1.27: (a) The picture of used ^{60}Co radioactive source and (b) Gamma-ray irradiation test setup. (c) Changes of scintillation glass before and after irradiation, numbering #1 to #6 from left to right.

Table 1.6: The performance of glass samples after gamma irradiation, with values in parentheses representing the performances before irradiation.

Sample index	Absorbed dose (Gy)	Transmittance (%@400 nm)	XEL peak (nm)	Light output (ph/MeV)	Decay time (ns)
#1	~9.4	73.2(78.5)	384(386)	1241(1604)	72(69), 578(575)
#2	~23.4	72.5(68.2)	388(388)	1233(1709)	78(71), 589(575)
#3	~47.3	61.2(75.2)	384(396)	1159(1608)	72(67), 575(572)
#4	~93.8	61.9(70.9)	390(396)	1059(1488)	78(71), 589(582)
#5	~191.3	57.4(68.9)	392(386)	957(1647)	68(82), 578(582)
#6	~375	47.7(60.8)	386(392)	701(1882)	66(63), 579(597)

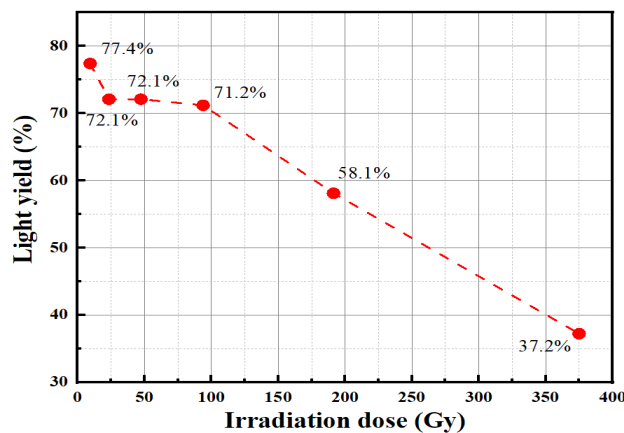


Figure 1.28: Gamma irradiation results showing the relative light yield of the scintillator as a function of irradiation dose. The light yield decreases gradually with increasing dose, reaching 58.1% at 191 Gy.

Scintillation performance was characterized through transmission spectra, XEL, light output, and decay time measurements as in Table 1.6. The maximum transmittance degradation was 14% - significantly less severe than proton irradiation at comparable doses (400 Gy). This difference likely stems from the lower dose rate and reduced ionization damage in gamma irradiation, as protons have higher linear energy transfer. The emission peaks remained stable (380-386

nm), consistent with proton irradiation results. Light output measurements using the same $^{137}\text{Cs}/\text{PMT}$ setup showed progressive degradation: 71% retention at 100 Gy and 37% at 375 Gy, matching proton irradiation trends. Decay times exhibited minimal variation, 87-89 ns fast component, 978-985 ns slow component, again consistent with proton irradiation observations. The gamma irradiation test results of the scintillator samples, showing the relative light yield as a function of accumulated dose, are shown in Figure 1.28. A significant degradation in light yield is observed with increasing dose, with the yield dropping to about 58.1.2% at 191 Gy. This corresponds to an expected total dosage (about 200 Gy [??]) of CEPC HCAL after 20 years of data taking.

The comparative analysis reveals that while both radiation types cause similar qualitative effects, gamma irradiation induces less severe degradation at equivalent doses. This suggests that the damage mechanism depends not only on total absorbed dose but also on radiation type and dose rate, with proton irradiation causing more severe ionization damage due to higher linear energy transfer.

1.4.2 Photon detector

Silicon Photomultipliers (SiPMs) have gained significant prominence in calorimetry applications owing to their compact form factor, high gain, low operating voltage, excellent radiation hardness, and insensitivity to magnetic fields. The CMS experiment at the LHC, for instance, is upgrading its endcap calorimeter with the High Granularity Calorimeter (HGCal) [29]. The hadronic part (CE-H) of the HGCal employs SiPMs to read out scintillator tiles. Designed to withstand high radiation fluxes while delivering superior spatial resolution for particle showers, the HGCal benefits from the inherent radiation tolerance and fine granularity of SiPMs. Similarly, the CALICE collaboration [10] has developed a highly granular calorimeter prototype for future collider experiments, utilizing SiPMs coupled to plastic scintillator tiles in electromagnetic calorimeters. Their scalability and compactness make SiPMs ideal for systems requiring particle flow algorithms (PFA).

The CMS experiment has further replaced its hybrid photodiodes (HPDs) with SiPMs in the barrel hadronic calorimeter [30], capitalizing on their improved timing resolution, higher photon detection efficiency (PDE), and enhanced radiation resilience. SiPMs are also being investigated for dual-readout calorimeters, where simultaneous measurement of scintillation and Cherenkov light from particle showers could improve energy resolution. Their fast response and precision enable discrimination between electromagnetic and hadronic shower components, thereby refining energy measurements—particularly for hadrons.

Commercially available SiPMs are offered by several manufacturers, including Hamamatsu (HPK), Onsemi (SensL), and Chinese producers such as CGN Capital Photonics Technology (CPT) and Rayquant (formerly Joinborn, JBT), as summarized in Table 1.7. Key SiPM parameters include pixel pitch size, pixel count, and active area, which directly influence performance metrics like dark current and gain.

The photon detection efficiency (PDE) of SiPMs is wavelength-dependent, typically peaking around 420 nm. For optimal performance, the PDE must align with the emission spectrum of the scintillator material. For example, the GFO glass scintillator (GS) emits at 400 nm, necessitating high PDE at this wavelength. Dark count rates, typically on the order of 100 kHz/mm², introduce noise and scale with pixel size, requiring careful mitigation in high-precision systems.

For the GS-HCAL application, the primary selection criteria include high PDE at 400 nm, high gain, low noise, and cost-effectiveness. Based on current performance metrics, the HPK S14160-3050 and NDL EQR20-11-3030 are promising candidates for prototype testing. However, rapid advancements in semiconductor technology may soon yield even more optimized SiPMs tailored for hadron calorimetry, warranting continued evaluation of emerging devices.

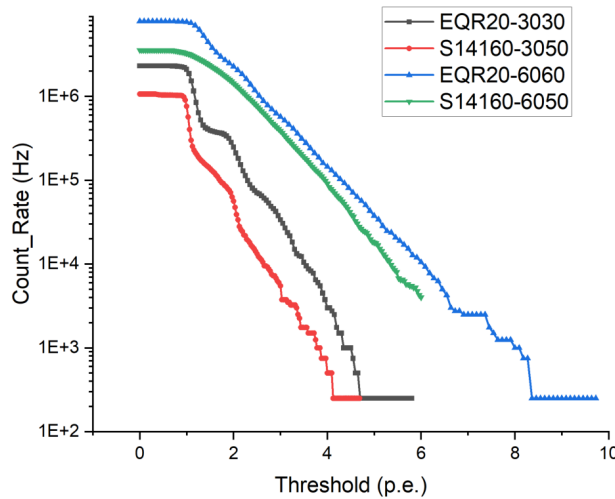
The high dark count rate (DCR) of SiPMs represents a critical consideration in applications involving weak signals. For GS-HCAL, the relatively low light yield of GS presents a challenge in achieving the desired 0.1 MIP detection threshold. Several methods exist for suppressing SiPM dark noise, including temperature reduction and electronic threshold adjustment. However, since the HCAL will operate at room temperature (approximately 21°C), which provides negligible noise reduction, threshold optimization emerges as the most practical approach for noise suppression.

Figure 1.29 illustrates the DCR characteristics as a function of threshold level (0–10 p.e.s). Measurements indicate a baseline DCR of 255 kHz/mm² at 0 p.e. threshold for the NDL EQR20 SiPM, compared to 112 kHz/mm² for the Hamamatsu S14160-3050 SiPM. Given the GS light yield specification of 100 p.e./MIP, a 0.1 MIP threshold corresponds

Table 1.7: The parameters of some typical commercial SiPMs.

Supplier	HPK			NDL		JBT
Type	S13360-3050CS	S13360-6050CS	S14160-3050HS	EQR20-11-3030-S	EQR20-11-6060-S	JSP-TP3050-SMT
Pitch [μm]	50	50	50	20	20	50
Active Area [mm^2]	3.0×3.0	6.0×6.0	3.0×3.0	3.0×3.0	6.24×6.24	3.0×3.0
Number of Pixels	3600	14400	3531	22500	97344	3364
Terminal Capacitance [pF]	320	1280	500	157.5	397	170 (fF)
Breakdown Voltage (V_B) [V]	53 ± 5	53 ± 5	38	27.2 ± 1	27.2 ± 1	24.6 ± 0.2
Maximum Operation Voltage (V_m) [V]	61	61	43	34.7 ± 1.6	34.7 ± 1.6	29.6
Recommended Operation Voltage [V]	$V_B + 3$	$V_B + 3$	$V_B + 2.7$	$V_B + 5$	$V_B + 5$	$V_B + 2$
Temperature Coefficient for V_B [mV/ $^\circ\text{C}$]	54	54	34	24.8	24.8	34.4
Peak Sensitive Wavelength [nm]	450	450	450	420	420	420
Peak PDE @ PSW [%]	40	40	50	47.8	47.8	35
Gain	1.7×10^6	1.7×10^6	2.5×10^6	8.0×10^5	8.0×10^5	2.1×10^6
Dark Count Rate (DCR) [kHz/ mm^2]	500–1500	2000–6000		150–450	150–450	120–270
Dark Current [μA]			0.6–1.8			0.65–1.44
PDE@400 nm [%]	35	35	47	45	45	33

to approximately 10 p.e.. The data demonstrate significant DCR suppression at higher thresholds: at 5 p.e., the DCR reduces to approximately 28 Hz/ mm^2 and 12 Hz/ mm^2 for the NDL and Hamamatsu devices, respectively. Extrapolating to the 10 p.e. operational threshold suggests even greater noise reduction for the standard $3 \times 3 \text{ mm}^2$ SiPMs employed in the HCAL design.

**Figure 1.29:** [to be updated] Dark counting rates of several SiPMs as a function of threshold.

1.4.3 Simulation study of attenuation length

[TODO: we have known issues to be fixed here. The simulated light yields n p.e./MIP is much less than actually measured. The initial scintillation light generation rate 1500 photons/MeV is assumed, we don't know if this is correct. The PDF actually used here is 60%, (not 40% in the text to be fixed), and the reflection efficiency used here is 90%, to be fixed.]

We conducted Geant4-based optical simulations of the GS coupled to SiPMs to characterize performance and identify optimization pathways. The standalone simulation framework enabled detailed photon tracking, with particular emphasis on light yield and attenuation length, which are key parameters for scintillator performance. The study focused on how GS attenuation length affects photon detection efficiency at the SiPMs, providing crucial data for material optimization. When ionizing particles deposit energy in the GS, a portion is converted to detectable visible light, similar to conventional scintillators. Our simulations modeled this full process from energy deposition to photon detection.

The simulation project consisted of three main components. The first part involved detector geometry, where we designed the GS geometry with SiPMs through a geometric interface. Based on the baseline design of the $40 \times 40 \times 10 \text{ mm}^3$ GS cell, we implemented one geometric configuration with SiPM coupling, a **single $3 \times 3 \text{ mm}^2$** SiPM positioned at the cell center. The entire periphery of the GS was wrapped in Teflon reflective film. In the simulation geometry, we avoided creating a small square groove on the GS for SiPM embedding, instead placing it on the readout PCB. This design choice eliminates the need for groove machining during GS cell production, significantly reducing manufacturing costs. All characteristics listed in Table 1.3 are incorporated into the simulation, with particular attention to attenuation length and emission peak.

The physics processes section include a physics list and optical processes. The physics list accounts for ionization, bremsstrahlung, multiple scattering, pair production, Compton scattering, and photoelectric effects. The optical processes cover scintillation and Cherenkov light generation, Rayleigh scattering, bulk absorption, and boundary processes. In the simulation, both the GS and SiPM are designated as sensitive detectors. The GS interacts with muons, while the SiPM detects emitted photons.

We conduct extensive validation to ensure the accuracy of simulation parameters and physical processes. Figure 1.30(a) displays the simulated photon arrival time distribution from the GS. The fast and slow time constants obtained through double exponential fitting correspond well with the values in Table 1.3. We then use a Cs-137 gamma source to simulate the response of reflective film reflectivity and SiPM active area on the final light yield. The gamma source is fixed at the GS center, coinciding with the SiPM position. Figure 1.30(b) presents the simulation results: black dots represent the effective light yield (assuming 40% PDE) for different SiPM active areas without reflective film; red dots show results with 80% reflectivity film; green dots correspond to 95% reflectivity. The results demonstrate that reflective wrapping increases light yield, with higher reflectivity yielding better results. Increasing the SiPM active area enhances effective light yield.

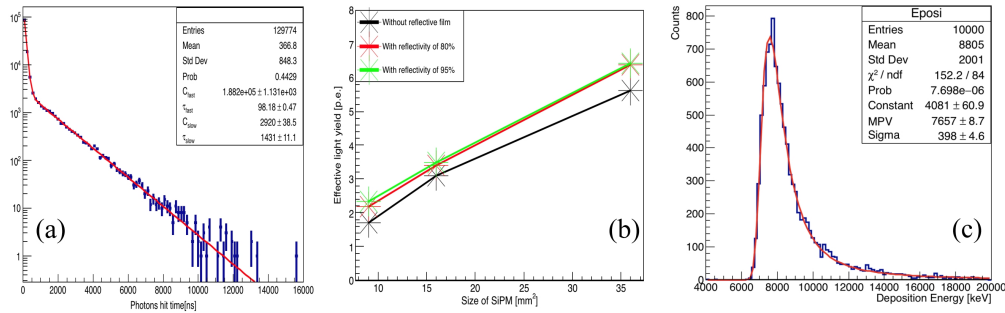


Figure 1.30: The results checked to validate the physical process in simulation, (a) Signal decay time (fast and slow components), (b) Effect of wrapping film with different reflectivity, (c) Muon deposited energy in GS cell (10mm thick).

Additional simulations are performed with 5 GeV muons uniformly and perpendicularly distributed on the GS cell. Figure 1.30(c) shows the deposited energy distribution, fitted with a Landau function, yielding a most probable value of 7.66 MeV/MIP. Our analysis revealed that attenuation length and light yield non-uniformity significantly impact light collection efficiency. Figure 1.31 compares energy spectra and 2D light collection efficiency distributions for attenuation lengths of 40, 60, and 80 mm. The results show that a GS tile of a $40 \times 40 \times 10 \text{ mm}^3$ area can be detected by a $3 \times 3 \text{ mm}^2$ SiPM with MPV of 23, 42, and 60 p.e./MIP, for attenuation lengths of 40, 60, and 80 mm, respectively.

The average effective light yield nearly doubles when the attenuation length increases by 20 mm. As shown in Figure 1.31, most photons are collected by SiPM surfaces due to the reflective film wrapping all GS surfaces except those coupled to SiPMs. Longer attenuation lengths yield higher collection efficiency and better uniformity across the SiPM surface. Based on deposited energy, GS properties, and cell geometry, we obtained the photon collection efficiency distribution within a GS cell. **[FIXME: improve the reasoning to demonstrate the capability.]** If the GS attenuation length exceeds 80 mm and GS couples to a $4 \times 4 \text{ mm}^2$ SiPM, or the attenuation length stays at 60 mm and PDE exceeds 50% coupling to a $6 \times 6 \text{ mm}^2$ SiPM, a light yield of about 100 p.e./MIP can be achieved.

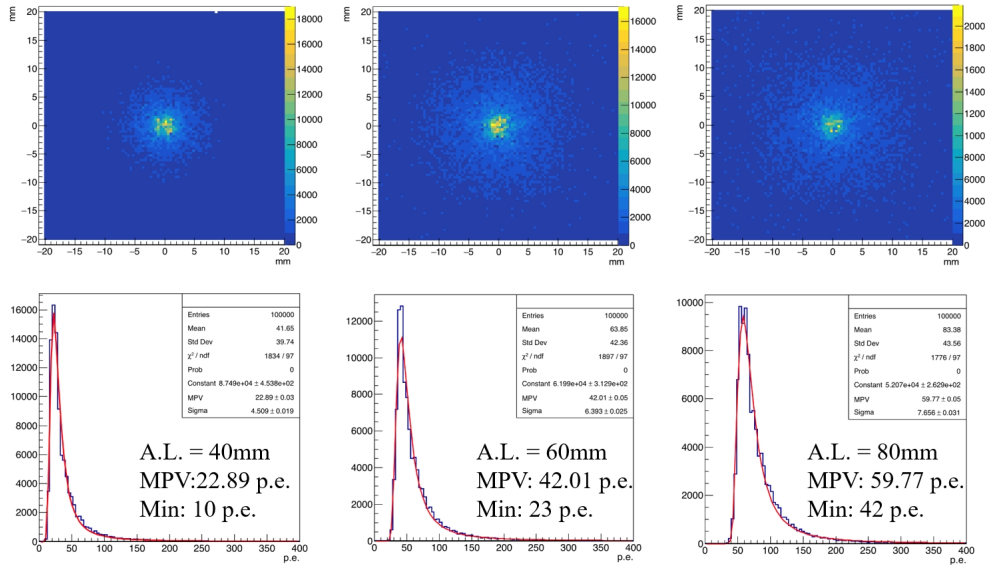


Figure 1.31: Simulation results of influence caused by attenuation length of GS. The energy spectrum (p.e.) and 2-D light collection efficiency distribution are compared for A.L. = 40 (left), 60 (middle) and 80 (right) mm respectively.

1.4.4 Measurements of GS with SiPM

GS samples of $40 \times 40 \times 10 \text{ mm}^3$ are prepared to evaluate the effective light yield under different configurations. Two distinct measurements are performed. one using 662 keV gamma rays from a ^{137}Cs source, and another utilizing cosmic ray muons depositing approximately 7.7 MeV per MIP. Both measurements employ SiPMs mounted at the center of GS cells on readout boards with pre-amplifiers, though with different sensor models optimized for each case.

For the ^{137}Cs measurement, the Hamamatsu HPK S13360-3025CS SiPM is selected, offering a PDE of 23% at 400 nm. The cosmic ray measurement uses the HPK S13360-3050PE SiPM with a PDE of 35%. Prior to these measurements, comparative tests of ESR and Teflon reflective films demonstrate superior performance of Teflon, showing approximately **XX% higher reflectivity** than ESR films. This enhancement stems from Teflon's softer composition, enabling better optical contact with the glass surface. In contrast, ESR films introduce slight air gaps and exhibit particularly poor reflectivity in the 380–400 nm range [31], which is around the peak region of the GS scintillation light spectrum.

The ^{137}Cs measurement employs Teflon films, while the cosmic ray test uses ESR films. In the ^{137}Cs setup, the radiation source is wrapped in aluminum foil with an aperture facing the SiPM, positioned at the center of the GS cell's opposite face. This configuration results in a minimal 10 mm propagation distance between source and sensor. The measured spectrum shows a photopeak at 679 ADC channels with a pedestal of 222 ADC channels, as shown in Figure 1.32. With a calibrated conversion factor of 61 ADC/p.e. and accounting for the 662 keV gamma energy versus 7.7 MeV per MIP, the derived light yield reaches 87 p.e./MIP.

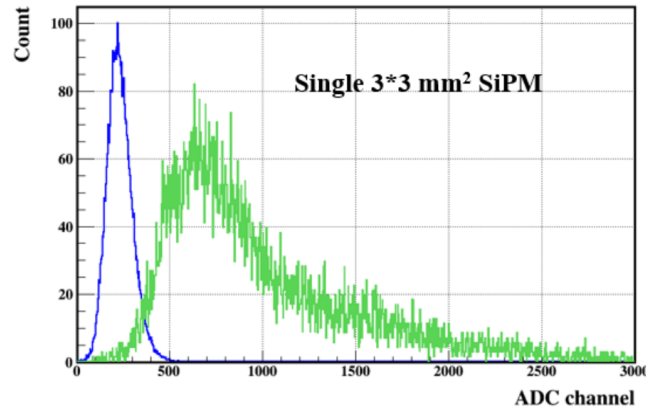


Figure 1.32: Measured ADC spectrum of GS cell with a SiPM (HPK S13360-3025CS) using ^{137}Cs radiative source, the light yield of GS is deduced to be 87 p.e./MIP.

The cosmic ray measurement configuration features two plastic scintillator trigger panels (top: $35 \times 5 \times 1 \text{ cm}^3$, bottom: $10 \times 5 \times 1 \text{ cm}^3$) surrounding the GS cell wrapped with ESR film. Coincident signals from both plastic scintillator panels initiate readout of the central detector, as shown in Figure 1.33. The cosmic ray test result shows that the GS+SiPM yields 48.6 p.e./MIP. **For comparison, GS cell wrapped with Teflon is under test, result will be added.**

The observed light yield discrepancy between the 87 p.e./MIP (^{137}Cs) and 49 p.e./MIP (cosmic) measurements arises from multiple factors. These include the differing reflectivities of Teflon versus ESR films, the varied PDEs of the respective SiPMs, and distinct event topologies. The ^{137}Cs measurement benefits from localized interactions near the SiPM, while cosmic muons distribute uniformly across the GS cell volume, making the result more susceptible to light attenuation effects.

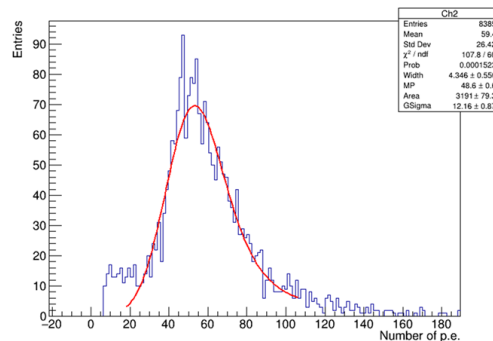
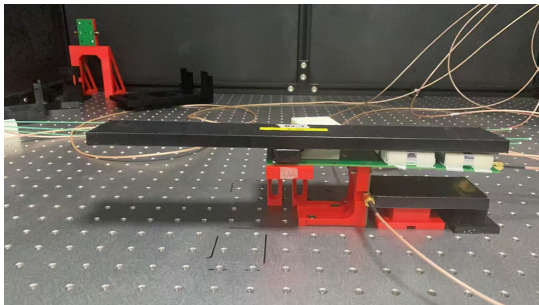


Figure 1.33: Left picture shows cosmic ray test platform for GS+SiPM cell, two plastic scintillators trigger panels (in black) are located at the top and bottom, while the GS and PCB with SiPM is mounted in the middle. Right plot shows measured light yield of GS ($40 \times 40 \times 10 \text{ mm}^3$) with a SiPM (HPK S13360-3050PE) is 49 p.e./MIP.

Based on current experience, the performance of the GS+SiPM is expected to be enhanced through the following optimizations:

- **Upgrade of SiPM Detectors:** Replacing the HPK S13360-3050PE SiPMs (PDE 35% at 400 nm) with HPK S14160-3050HS models (PDE 47% at 400 nm), which offer a 34% improvement in photon detection efficiency.
- **Enhanced Reflective Wrapping:** Substituting ESR films with Teflon films for GS wrapping, which is anticipated to increase light collection efficiency by approximately 20%.
- **Optimization of Glass Scintillator:** Through ongoing material research, a 30% increase in the light yield of the GS is projected over the next few years.

These improvements are calculated to yield a combined light yield of about 102 p.e./MIP, derived from the product of current performance from cosmic ray test 48.6 p.e./MIP and the multiplicative factors of each enhancement: $48.6 \times 47\%/35\% \times 1.2 \times 1.3 \sim 102 \text{ p.e./MIP}$. This result demonstrates that the design specification of 100 p.e./MIP is achievable with the proposed upgrades, ensuring the system meets the required performance benchmarks for precision calorimetry.

1.4.5 Calibration

1.4.5.1 Calibration using physics processes

Isolated hadrons Several physics processes can produce isolated hadrons, such as hadronic τ decays in $Z \rightarrow \tau^+\tau^-$ events or isolated hadrons within jets. By leveraging particle flow reconstruction, the tracker can precisely determine the energy of these hadrons. Applying a veto on energy deposits in the ECAL allows for the selection of pure hadronic showers in the HCAL. The E/p ratio of these showers can then be used for calibration purposes. This method is particularly suitable for time-dependent monitoring of the HCAL response, though not for absolute channel-by-channel calibration.

Di-muon events ($e^+e^- \rightarrow Z \rightarrow \mu^+\mu^-$) The global calibration of the GS-HCAL can be performed using minimum ionizing particle (MIP) signals from prompt muons produced in collisions. These muons, identified by the inner tracker and muon chamber systems, predominantly lose energy through ionization, with a response that scales nearly linearly with their path length through the HCAL cells. The $e^+e^- \rightarrow Z \rightarrow \mu^+\mu^-$ process provides an ideal source of such high-momentum isolated muons. Figure 1.34 shows the kinematic distributions of muons at $\sqrt{s} = 91$ GeV.

During Z-pole running, this process occurs at a rate of 584 Hz at the design instantaneous luminosity. A conservative estimate yields 47 events per hour within a $\Delta\phi \times \Delta\cos\theta = 0.018 \times 0.018$ acceptance window, corresponding to one 4×4 cm² GS cell at the central barrel HCAL surface. The event rate increases significantly with $\cos\theta$. Assuming regular two-week calibration runs in Z mode (16 hours per day), we can collect 4.71×10^8 di-muon events for HCAL calibration, achieving a statistical precision better than 1%.

Resonant jets ($e^+e^- \rightarrow Z \rightarrow q\bar{q}$) The dominant process in Z-pole operation, $e^+e^- \rightarrow Z \rightarrow q\bar{q}$, provides resonant jets that enable combined ECAL and HCAL calibration. The total reconstructed energy $E_{\text{tot}} = a \times E_{\text{ECAL}} + b \times E_{\text{HCAL}}$ should match the known Z boson energy. This method serves as an important cross-check of detector performance across the full acceptance by examining objects in different phase space regions.

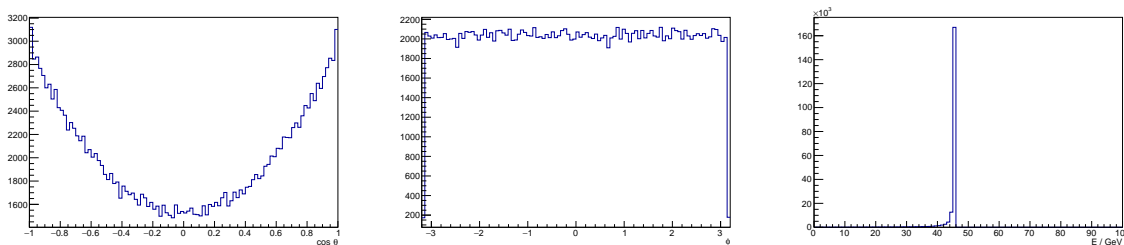


Figure 1.34: Distributions of $\cos\theta$ (left), ϕ (middle) and energy (right) for the muon in $e^+e^- \rightarrow \mu^+\mu^-$ process, $\sqrt{s} = 91$ GeV.

1.4.5.2 Hardware calibration

System design The HCAL must maintain stable performance over extended periods of operation, despite potential degradation of the GS and SiPM components due to radiation damage or aging effects. A dedicated calibration system is therefore essential for monitoring key parameters including pedestal levels, gain characteristics, and response linearity.

The calibration system employs an LED-based design, with schematic diagrams shown in Figure 1.35. The system architecture features an LED and SiPM mounted on a common PCB, with the LED positioned adjacent to the SiPM. The GS contains precisely machined recesses to accommodate these components while maintaining optical coupling. The LED is driven by a programmable pulsed power supply, allowing precise control of light intensity through adjustable voltage and pulse width settings. Photons emitted by the LED propagate through the GS and are detected by the SiPM, enabling characterization of both the GS optical properties and SiPM performance.

This compact single-SiPM configuration provides several advantages. The simplified geometry improves mechanical reliability while maintaining calibration accuracy. The design also facilitates comprehensive testing of the GS light transmission characteristics and attenuation length, as well as SiPM parameters including photon detection efficiency and

gain stability. The system's ability to monitor these parameters simultaneously ensures consistent HCAL performance throughout its operational lifetime.

For practical implementation, two GS cell layouts have been developed. In the primary design, both SiPM and LED are mounted within precision-machined recesses in the GS. An alternative configuration, positions the SiPM within a PCB cavity rather than the GS itself. This approach simplifies GS manufacturing while maintaining calibration capability through a secondary PCB that hosts both the LED and SiPM.

Electronics and control The calibration system comprises two main subsystems: the front-end SiPM board and the bias power control board. The front-end board houses the LED and SiPM in their operational configuration, while the control board generates the precise voltage pulses required for LED operation. These pulses serve dual purposes: driving the LED to produce calibration light and triggering the DAQ system to record SiPM responses.

System operation is managed through the DAQ interface, which coordinates pulse generation, data acquisition, and subsequent analysis. The calibration protocol involves scanning through predefined voltage and pulse width settings while recording the corresponding SiPM responses. This data enables determination of critical parameters including GS light yield, attenuation characteristics, and SiPM gain stability.

The photon propagation within the GS involves multiple reflections before detection, making the system sensitive to changes in both the scintillator's optical properties and the SiPM performance. This comprehensive sensitivity allows the calibration system to track long-term performance variations of the entire GS cell assembly. Further studies will optimize the calibration procedures to account for anticipated aging effects during prolonged detector operation.

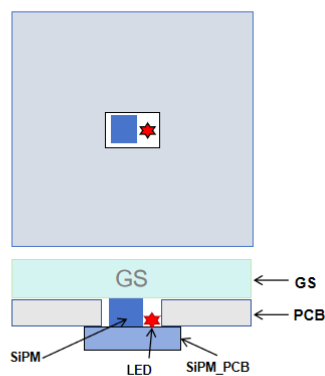


Figure 1.35: Schematic diagram of the calibration system.

1.4.6 Readout electronics for R&D

The HCAL design incorporates more than five million channels of SiPMs, making the front-end electronics crucial for signal processing and readout. The electronic chain consists of several key components: a stable, low-noise bias voltage supply to provide the SiPM operating voltage; a charge-sensitive pre-amplifier to amplify the small current pulses from the SiPMs to measurable levels; and a shaping stage to optimize the signal-to-noise ratio and timing resolution through analog or digital techniques. Subsequent processing includes discriminators for photon counting and timing measurements by generating digital pulses when signals exceed predefined thresholds, along with time-to-digital converters (TDCs) for precise time measurements relative to a reference signal. The system also incorporates analog-to-digital converters (ADCs) to digitize pulse amplitudes for energy measurements, with all channel data being collected and processed by a centralized data acquisition (DAQ) system. The design of each component emphasizes stability, low noise, and high channel density to meet the demanding requirements of the HCAL system.

The CEPC detector system will ultimately feature a unified electronics design, but its full implementation remains years away. To enable immediate SiPM characterization and HCAL prototype testing, a customized front-end electronics (FEE) solution is urgently required. This interim system must accommodate diverse commercial SiPMs while serving as

a design reference for the final HCAL electronics. Key requirements include dynamic range (0.1-100 MIPs, with 1 MIP \approx 100 p.e.), charge and timing resolution, event rate capability, and power efficiency—parameters detailed in Table 1.8. Commercial solutions prove inadequate due to their lack of universality; most manufacturer-provided pre-amplifiers are single-channel and incompatible across SiPM brands. The HCAL R&D requires a multi-channel FEE design to enable simultaneous testing of multiple SiPMs, maintaining flexibility for various readout configurations during prototype studies.

Table 1.8: SiPM characteristics that drive the requirements for the readout electronics design.

Item	Requirement
Charge dynamic range	0.8~800 pC (10~10000 p.e., 0.1~100 MIPs) @ 100 p.e./MIP
Timing measured range	TBD from electronics
Charge resolution	0.8 pC (10% of 1.0 MIP, i.e. 10 p.e.)
SiPM capacity	≤ 100 pF
SiPM gain	$\geq 5 \times 10^5$
Average event rate/channel	Berral mean 0.24 kHz, Endcap mean 1.45 kHz
Max event rate/channel	Berral max 6.2 kHz, Endcap max 46.3 kHz
Rising edge	2~3 ns
Typical signal	2~3 mV/p.e.
Other requirements	FEE gain adjustable in 2/3 levels, Signal saturation protection HV independent, adjustable by layer, Random trigger (for test) Calibration function

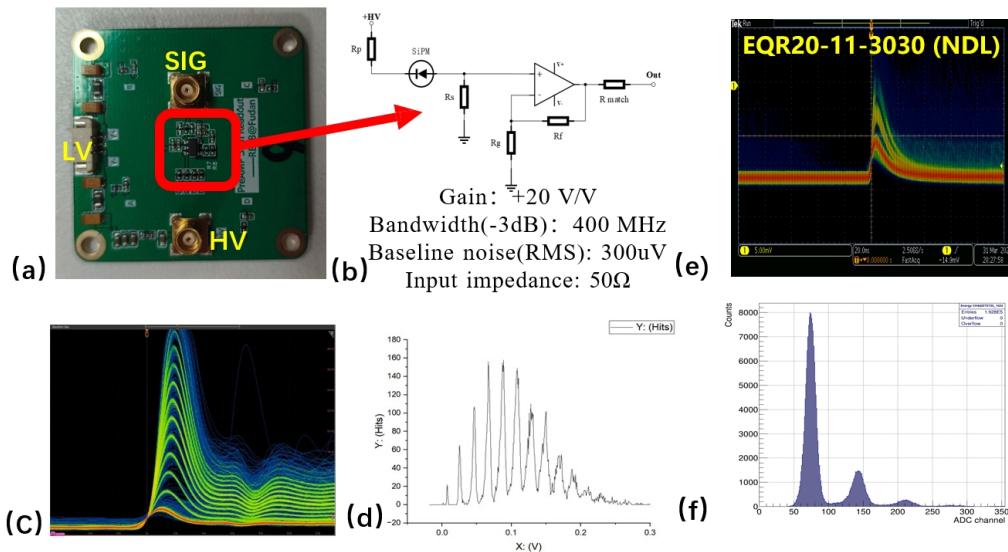


Figure 1.36: The pre-amplifier for HCAL SiPM study. (a) one pre-amplifier channel PCB coupling to GS cell. (b) the schematic diagram of the pre-amplifier. (c) and (d) the performance of the pre-amplifier. (e) Signal of one 3×3 mm² SiPM (EQR20 11-3030D-S) coupling with a readout PCB. (f) ADC distribution of dark noise of a 3×3 mm² NDL SiPM.

Optimal SiPM performance demands careful FEE implementation to address gain stability, noise reduction, and timing resolution. Critical design aspects include impedance matching to minimize signal reflections, temperature compensation (or active cooling) to stabilize gain and dark count rates, and wide bandwidth (>400 MHz) to capture nanosecond-scale pulses. The FEE must handle a broad dynamic range (input signals up to 170 mV) while maintaining low noise levels (<1 mV baseline). The signal from the SiPM is first amplified by a dedicated pre-amplifier before being processed by the readout electronics. Figure 1.36 shows the pre-amplifier developed for the HCAL SiPM study. The pre-amplifier is implemented on a compact PCB (Figure 1.36a), designed to couple directly to the GS cell, and its schematic diagram is shown in Figure 1.36b. The circuit features a gain of ± 20 V/V, a bandwidth of 400 MHz, and a baseline noise of 300 μ V RMS, with an input impedance of 50 Ω . The performance of the pre-amplifier is demonstrated in Figure 1.36c and 1.36d, showing clean multi-photoelectron signals. Figure 1.36e displays a typical waveform from a 3×3 mm² NDL

SiPM (EQR20-11-3030D-S) coupled with the pre-amplifier, while Figure 1.36f presents the ADC spectrum of the SiPM dark noise, demonstrating well-separated photoelectron peaks.

For the HCAL application, the FEE must integrate low-noise amplification, noise filtering (to suppress dark counts and afterpulsing), and pulse shaping while remaining adaptable to potential temperature control systems. The implemented solution achieves this through compact, high-speed circuitry that preserves signal integrity across the full dynamic range. This design not only meets immediate testing needs but also informs the development of the final CEPC electronics system, ensuring compatibility with future domestic and international SiPM technologies.

1.4.7 Prototype

We present a detailed description of the simulation, design, and test plan for the 0.6 m^3 glass scintillator analog hadron calorimeter (GS-AHCAL) prototype. The prototype features a steel - scintillator sandwich structure, where the scintillator planes are segmented into square tiles, each individually read out by SiPM. The steel plates measure $52\text{ cm} \times 52\text{ cm}$ in width and have an average thickness of 9.8 mm. We utilize standard S304 steel, which is a composite material composed of iron, carbon, manganese, nickel, phosphorus, and sulfur.

For the GS-AHCAL prototype, we have two key goals. Firstly, we aim to conduct large-scale tests on the novel glass scintillator (8112 tiles), identify any critical operational challenges, develop comprehensive quality control procedures, and establish reliable calibration concepts based on test bench data. Secondly, we intend to accumulate extensive data samples of hadronic showers from the GS-AHCAL in test beams. These samples are crucial for exploring hadronic shower shapes and validating simulation models, as such information cannot be obtained from existing calorimeter data. Moreover, the test beam data samples are invaluable for studying and optimizing PFA.

1.4.7.1 Simulation of GS-HCAL prototype

The standalone simulations of the GS - AHCAL prototype have been carried out. These simulations were conducted to assess the energy coverage of an 80 - GeV proton beam for a module size of $3.24 \times 3.24\text{ m}^2$ (comprising 81×81 tiles) and to analyze the pion shower profile with 80 layers. The simulation results indicate that the majority of energy deposition occurs predominantly along the center of the proton beam. Even with 48 sampling layers, an 80 GeV pion beam still experiences energy leakage in the longitudinal direction.

Figure 1.37 depicts the comparison between energy coverage and the total number of cells. It is evident that beyond a cross section of 13×13 cells, the difference in leakage energy becomes less significant. However, the number of detector cells increases rapidly. A 95% energy coverage rate was determined to be acceptable. Taking both cost and performance into account, the prototype size of $13\text{ cells} \times 13\text{ cells} \times 48\text{ layers}$ was selected. Figure 1.37 also shows the deposited energy of an 80 GeV proton beam as a function of the prototype size. The deposited energy for the $13 \times 13 \times 48$ prototype size is already approaching the level of full energy deposition.

Owing to the relatively small size of the prototype, energy leakage is inevitable. This results in a degradation of energy resolution when compared to the full sized AHCAL. Figure 1.38 presents the energy resolution curve and linearity of the prototype when irradiated with a proton beam.

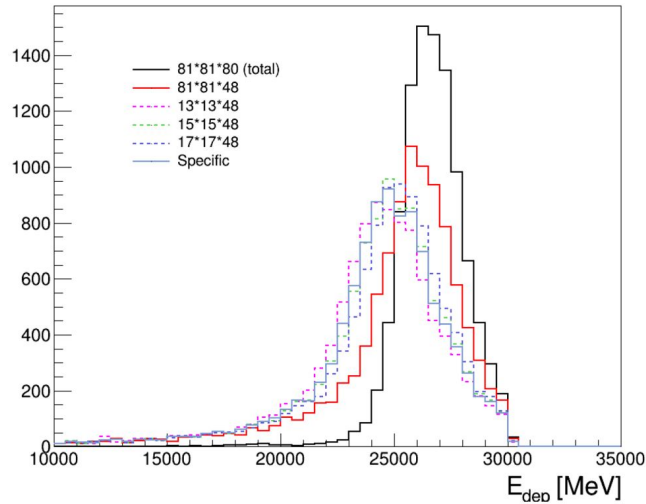


Figure 1.37: Distribution of deposited energy in prototype with different size using 80 GeV pion for simulation.

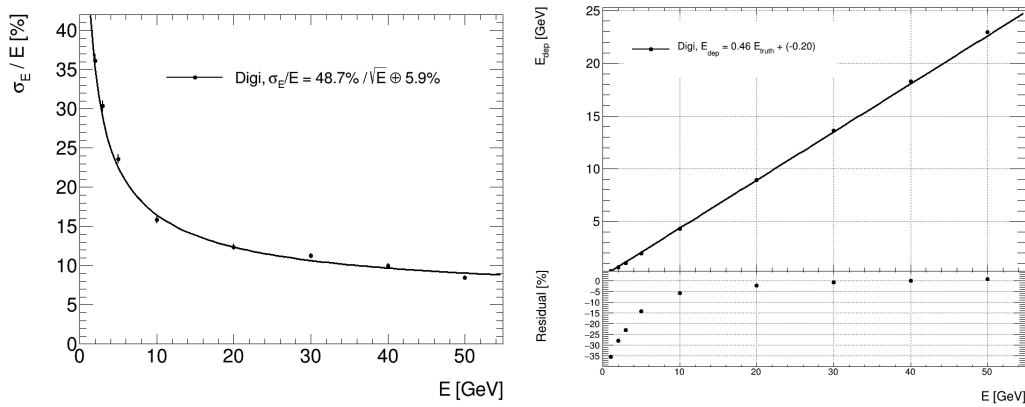


Figure 1.38: Energy resolution and energy linear of GS AHCAL prototype based on simulation.

1.4.7.2 Design and construction plan of GS-HCAL prototype

The GS-AHCAL prototype will be constructed with a total of 8112 glass scintillator (GS) cells, each measuring 4 cm × 4 cm × 1 cm. Each cell will be optically coupled to one 3 × 3 mm² SiPMs for readout. The detector will feature a cross-sectional area of 52 × 52 cm², composed of 48 alternating layers of GS cells and stainless steel absorbers, resulting in an overall thickness of approximately 130.6 cm. Figure 1.3 illustrates the coupling scheme between the GS cells and SiPMs, where each GS cell is paired with one SiPM for signal collection. Figure 1.39 depicts a single layer of the prototype, consisting of 169 individually instrumented GS cells.

The assembly process involves adhering each GS cell to a printed circuit board (PCB). Each SiPM, along with a dedicated LED for calibration purposes, is soldered onto a small daughter board, which is then integrated with the main layer PCB. The entire active layer is enclosed between upper and lower stainless steel covers, forming a modular cassette that simplifies installation and protects the electronics and scintillators. Figure 1.39 showcases the preliminary mechanical design of the 13 × 13 cell × 48 layer prototype, totaling 8112 channels. The structure alternates between 48 sensitive GS layers and 48 stainless steel absorber layers, secured within a slotted stainless steel frame. This modular design allows for flexible adjustments and straightforward removal of individual layers for maintenance or upgrades.

A 2-mm gap is maintained between adjacent layers to accommodate steel plate unevenness and ensure smooth cassette insertion, particularly critical for maintaining alignment with vertical beam directions. The light output from the GS tiles is detected by NDL-SiPM photodetectors, which offer high gain (>1E5) and excellent photon detection efficiency (>30%), as demonstrated in previous experiments such as GECAM and JUNO-TAO. A total of 8112 SiPMs will be deployed in this prototype, selected for their optimal cost-performance ratio.

GS AHCAL prototype calibration A set of blue light LEDs will be employed to calibrate the SiPMs and the associated electronics. At the SiPM's operational point, multiple key characteristics of the SiPMs will be measured. When the LEDs are set to low light intensities, pulse height spectra, which are crucial for gain calibration, will be recorded. Exceptional resolution is of utmost importance for calorimetric applications as it enables self-calibration and continuous monitoring of each channel. Additionally, the response function of each SiPM across the entire dynamic range, from zero to saturation, will be recorded.

GS AHCAL prototype ASIC The CEPC electronics group is developing a new version of ASIC chips for both the ECAL and HCAL. The GS-AHCAL prototype will utilize this new type of ASIC, named ChoMin. This 36-channel ASIC chip is being designed to consume only 15 mW of power per channel. Such low power consumption significantly reduces the cooling requirements for the GS-AHCAL prototype, making the overall system easier to manage.

Reflective film of glass scintillator A comparative assessment was carried out on ESR films, titanium oxide coatings, and Teflon films as reflective coatings for the glass scintillator. The experimental results clearly indicate that both the titanium oxide coatings and the Teflon films exhibit superior reflectivity performance when applied to the glass scintillator. In contrast, the ESR reflective films show relatively inferior reflection performance for the glass scintillator. These findings are crucial for optimizing the light collection efficiency of the scintillator.

GS AHCAL prototype cooling To verify the effectiveness of the final cooling solution for the GS-AHCAL, the prototype detector will be cooled using cooling water. This approach allows us to master all the technical aspects necessary for the full-scale GS-AHCAL cooling system. The prototype will be equipped with a compact industrial water chiller that is connected to the prototype's cooling water pipes. By precisely regulating the flow rate and temperature of the cooling water, efficient cooling of the prototype detector is achieved. The black pipes shown in Figure 1.39 form the cooling water piping system of the prototype, which plays a vital role in maintaining the detector's optimal operating temperature.

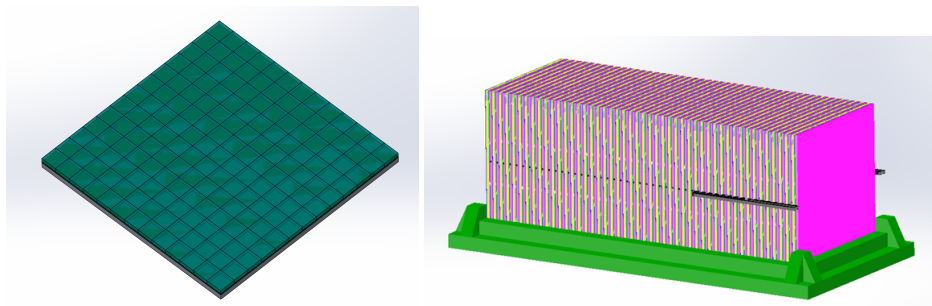


Figure 1.39: one layer and whole size of GS-AHCAL prototype.

1.4.7.3 Beam test consideration

A mini-prototype with a configuration of 3 cells \times 3 cells \times 7 layers has been designed and is currently under construction. The beam test of this mini-prototype is scheduled to be carried out at CERN in October 2025. According to the plan, the full-scale prototype mentioned above is expected to be completed by the end of 2026, and cosmic ray tests and/or beam tests are planned for 2027. The cosmic ray experiment will be conducted at the Institute of High Energy Physics (IHEP) in China. CERN is the preferred location for the beam test because it can supply muon, pion and electron beams with energies ranging from a few GeV to several hundreds GeV. In case that CERN beam test is not available in 2027, alternative options are available. One option is China Spallation Neutron Source (CSNS), which can provide a 1.6 GeV proton beam. Another alternative is the proton beam facility at the University of Tokyo in Japan.

A dedicated beam testing platform will be constructed. This platform is designed to have a movement range of ± 25 cm in both the vertical and horizontal directions with a precision better than 1 mm, a rotation range of ± 30 degrees, and a load-bearing capacity exceeding 5 tons. It will also be equipped with a remote control system. During the beam testing

process, the prototype will be placed on this platform, enabling highly convenient adjustment of the beam's hit position on the prototype.

1.5 Simulation and performance

The primary objective of this section is to validate that the GS-HCAL design meets the CEPC physics program's core performance criteria, including hadronic energy resolution, linear response across the energy spectrum, and mitigation of beam-induced background effects on signal reconstruction. Leveraging extensive simulation studies in the absence of prototype data, we demonstrate the design's compliance with these requirements.

This section describes the GS-HCAL's global performance, focusing on energy linearity, resolution parameterization (with emphasis on the constant term), and Boson Mass Resolution (BMR) studies for benchmark physics process. We then analyze beam-induced background simulations to quantify their impact on the calorimeter and outline mitigation strategies. These investigations confirm that the GS-HCAL layout and readout architecture reliably satisfy the CEPC environment's stringent requirements and physics objectives.

1.5.1 Simulation and digitization

The energy linearity and resolution of the GS-HCAL are estimated using Geant4 simulation within the CEPCSW framework. To study the intrinsic energy response of the GS-HCAL, all inner sub-detectors are removed. A digitization model is then constructed, taking into account the following factors:

- Birks constant. Currently a preliminary value of $C_{Birks} = 0.01$ is used. A measurement using heavy ion beam is being planned for more accurate determination.
- Light yield. Based on measurements of GS samples, the intrinsic MIP light yield can reach to approximately 2000 ph/MeV. Consequently, the detected light yield is expected to be at least 100 p.e./MIP. which meets the requirements related to descent signal to noise ratio and 0.1 MIP threshold.
- Attenuation length. 6 cm attenuation length is expected according to current measurements. However, more in-depth studies of the GS properties are needed.
- Threshold. Through scanning the impact on energy resolution, a 0.1 MIP threshold is determined.
- SiPM response. The response of the SiPM is also incorporated into the model
- Electronic system. The characteristics of the electronic system are considered.
- After calibration, Other factors are considered as having negligible effects.

1.5.2 Single hadron energy resolution

This model yields an estimated energy resolution of $\sigma_E/E = 29.8\%/\sqrt{E} \oplus 6.5\%$ and an energy linearity within 2% before calibration, as shown in Figure 1.40. The default physics list used is 'QGSP-BERT', and other physics lists have been tested. The relatively large constant term in the energy resolution is attributed to the longitudinal leakage in this $6\lambda_I$ design, which is constrained by the total detector volume and cost. This result outperforms that of traditional HCALs, which typically have an energy resolution of $\sigma_E/E = 60\%/\sqrt{E} \oplus 3\%$.

In the CEPC collision environment, as depicted in Figure 1.41, more than 98% of hadronic objects in the final state have energies of less than 60 GeV. This enables the GS-HCAL to achieve optimal energy resolution within physics of interest for the CEPC.

Although the current digitization model provides a conservative estimate of 6.5% for the constant term in the energy resolution, it is crucial to recognize that several contributing factors can be mitigated through calibration and reconstruction enhancements. The preliminary simulation incorporates non-optimized parameters, such as a short light attenuation length and longitudinal leakage effects. However, future calibration procedures are expected to partially compensate for these issues.

A detailed simulation study was performed to evaluate the impact of various effects on the single hadron energy resolution of the GS-HCAL. As shown in Figure 1.42, three key factors were investigated, the light yield and energy

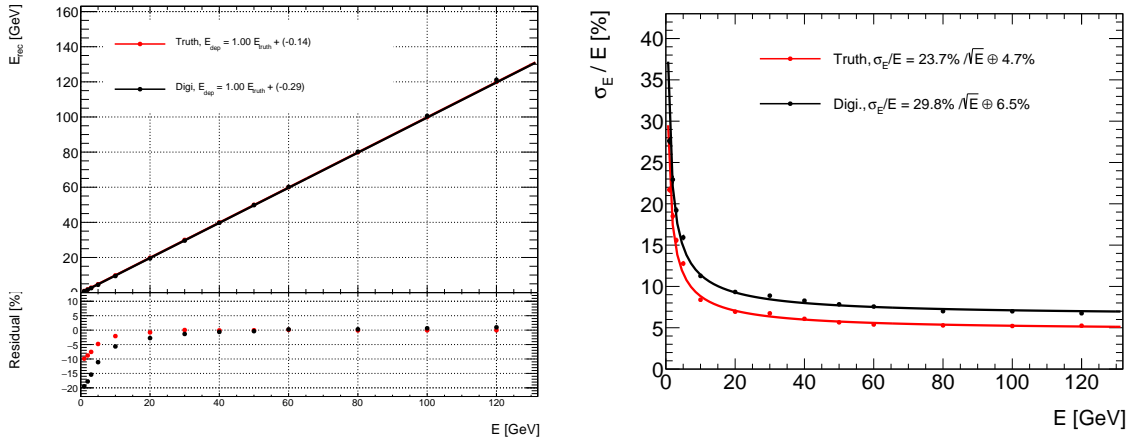


Figure 1.40: Energy linearity and energy resolution of GS-HCAL with the digitization model.

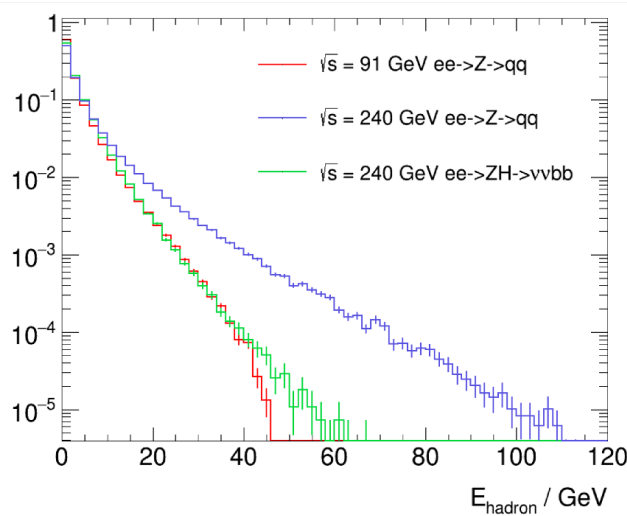


Figure 1.41: Hadronic objects energy distribution in the most energetic processes in e^+e^- collision.

threshold, the light attenuation length of the GS, and the Birk's constant used in the modeling of scintillation quenching. These parameters were found to significantly affect the calorimeter performance, particularly in the low-energy regime, highlighting the importance of optimizing the scintillator properties and calibration methods for precise energy measurement.

1.5.3 Understanding of large constant term

In hadronic calorimetry, the energy resolution is typically characterized by the formula,

$$\frac{\sigma_E}{E} = \frac{a}{\sqrt{E}} \oplus b \oplus \frac{c}{E},$$

where a represents the stochastic term, b is the constant term, and c is a noise term. A sampling hadronic calorimeter GS-HCAL showed a surprisingly large value of b when compared to a similar detector PS-HCAL. Initially, the difference was a cause for concern, as a large constant term might indicate fundamental problem like non-uniformities or calibration errors. However, further investigations provided an alternative explanation: in the GS-HCAL, the calorimeter depth was sometimes insufficient to contain hadronic showers, resulting in energy leakage that artificially increased the constant term. Here details how this conclusion was reached and illustrates the key findings with relevant figures.

Once we recognized that the depth of the GS-HCAL geometry under consideration might be insufficient, an alternative explanation emerged. Specifically, for hadronic showers that initiate late or develop with great depth, the GS-HCAL configuration could permit a substantial portion of the energy to escape. To verify the hypothesis that longitudinal leakage was the cause of the observed discrepancy, we increased the depth of the GS-HCAL from 48 layers ($6 \lambda_I$) to 80 layers (10

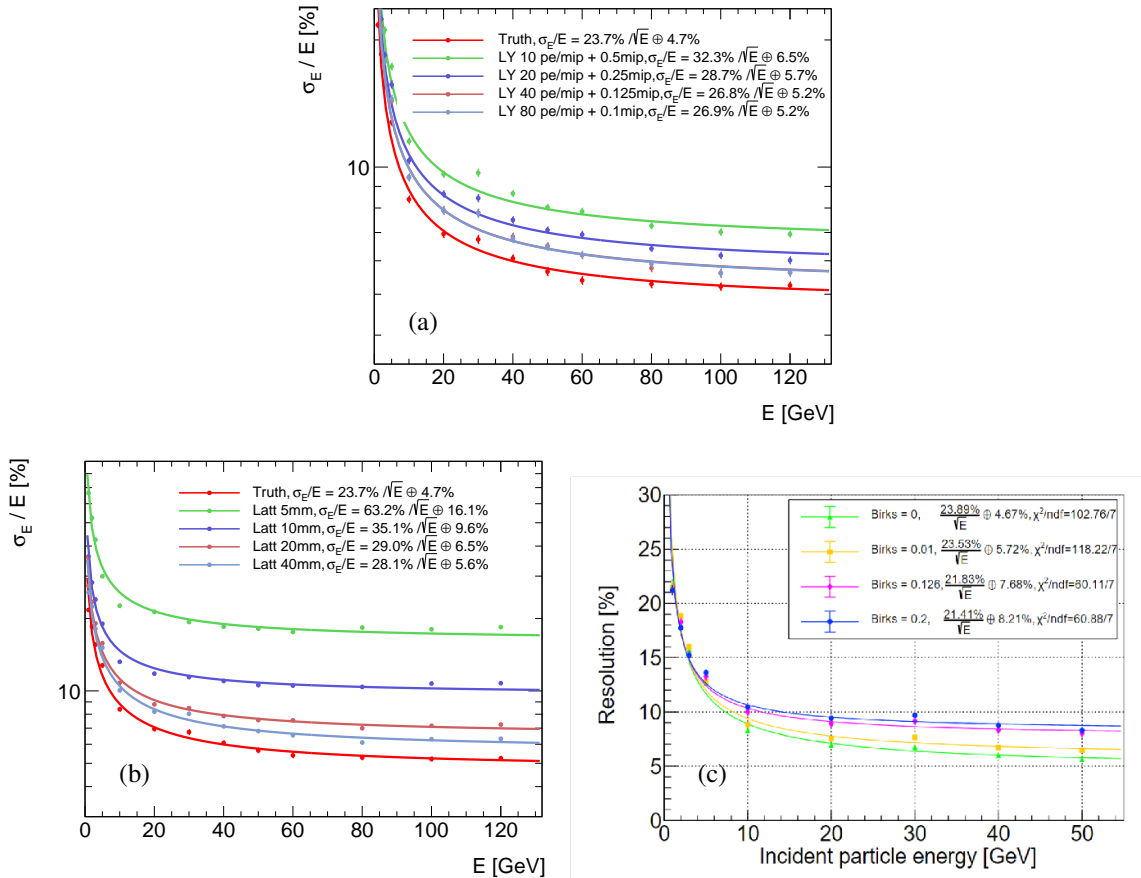


Figure 1.42: The simulated energy resolution with varies of (a) light yield and energy threshold, (b) glass scintillator attenuation lengths, (c) Birk's constants.

λ_I). The results of this adjustment are presented in Figure 1.43. With 48 layers, the calorimeter generated a pronounced tail in the energy distribution at higher beam energies, leading to an extracted constant term of approximately 4.7%. However, when the calorimeter depth was extended to 80 layers, this tail decreased significantly, and the constant term dropped to around 2.9%. This improved value is in good agreement with the range commonly observed in similar calorimeters.

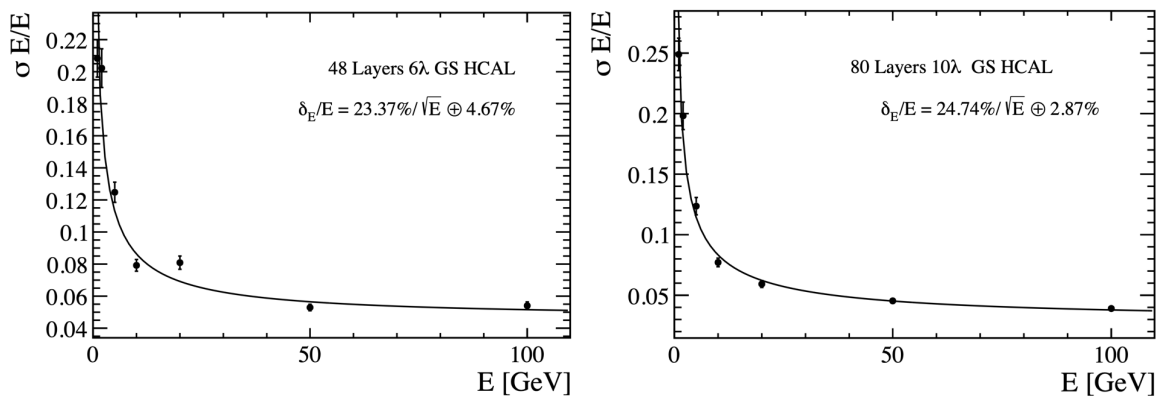


Figure 1.43: Comparison of two GS-HCAL configurations with different depths. A shallower setup with 6 λ_I (left) yields a pronounced high tail in the energy resolution and a large constant term. A deeper setup with 10 λ_I (right) effectively contains the showers, reducing the tail and lowering the constant term to a more typical value.

The significant improvement in the constant term upon increasing the depth of the GS-HCAL supported the hypothesis that shower leakage, rather than an intrinsic design flaw, was responsible for the inflated constant term. The deeper calorimeter configuration effectively contained the hadronic showers, demonstrating the performance characteristics of a

well - functioning hadronic detector.

While increasing the depth provided a direct solution, it was also essential to demonstrate that event selection methods could restore a more typical constant term without physically modifying the detector. Figure 1.44 shows two such selection techniques applied to 48 layer GS-HCAL configuration. One method involved using only lower energy pions, which have a reduced likelihood of penetrating the full depth and escaping. The other required the hadronic shower to initiate within the first few layers of the detector. Both approaches led to a reduction in the fitted constant term, with values ranging from approximately 2.9% to 3.4%. These results closely matched the expected performance for a detector of this design, eliminating the need for more complex explanations. Once events affected by leakage were removed or minimized, the seemingly large constant term was significantly reduced.

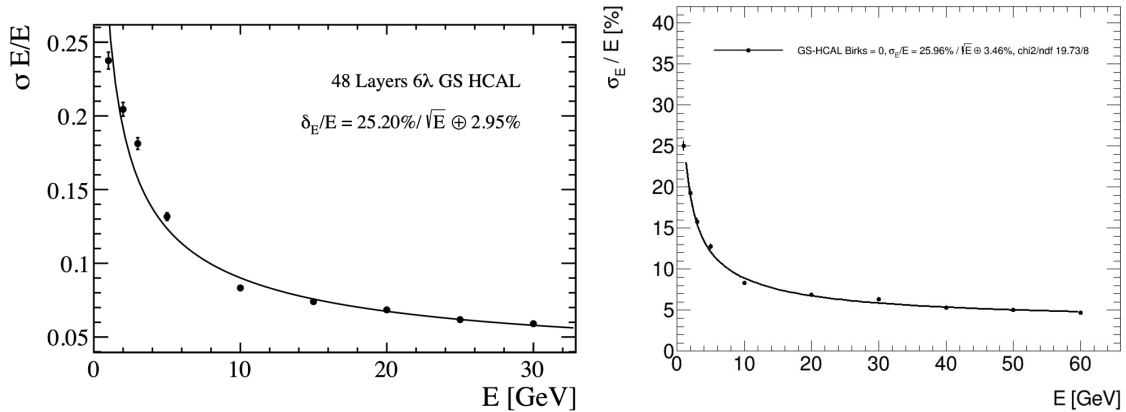


Figure 1.44: Reduction of the constant term in the shallower configuration through selective event removal. Focusing on lower beam energies (left) or ensuring the shower starts in the first few layers (right) mitigates leakage, lowering the constant term.

As the study for the CEPC HCAL progresses, a multifaceted approach is being deployed to reduce the constant term below the 3% target by integrating advanced energy compensation and containment strategies. Central to this effort is the development of longitudinal energy-weighting algorithms that dynamically adjust for non-uniform light yield across shower depths, combined with precision corrections for position-dependent light-collection efficiency derived from optical simulations and prototype validations. Machine learning techniques are further leveraged to correlate 3D shower topologies with Geant4-simulated energy deposition, enhancing reconstruction accuracy.

1.5.4 Performance

The reconstruction performance of physical events is evaluated through PFA which synthesizes information from tracker, calorimeters and other sub-detector systems. The Higgs boson decay channel $H \rightarrow gg$ serves as the benchmark process to quantify the detector performance.

Event generation is performed using Whizard v1.9.5 with next-to-leading-order matrix elements, followed by full detector response simulations using Geant4 v10.7 [??] within the CEPCSW framework. Digitized signals from tracker hits and calorimetric energy deposits are reconstructed into charged particle trajectories and electromagnetic/hadronic clusters, respectively, with reconstruction algorithms detailed in Software Chapter [add a link]. By aggregating the four-momenta of all reconstructed particles, the fitted Higgs mass in gluon pair final state is 126.32 ± 0.04 GeV, $\sigma(m_{jj}) = 4.90 \pm 0.04$ GeV. The Higgs boson invariant mass resolution (BMR) of 3.88% is achieved across the 120–130 GeV mass range, as shown in Figure 1.45.

1.6 Alternative solutions

As backup solutions, two alternative approaches have been studied systematically within the context of the CALICE collaboration in the past two decades: the Digital HCAL (DHCAL) [32, 33] or the Semi-Digital HCAL (SDHCAL) [13,

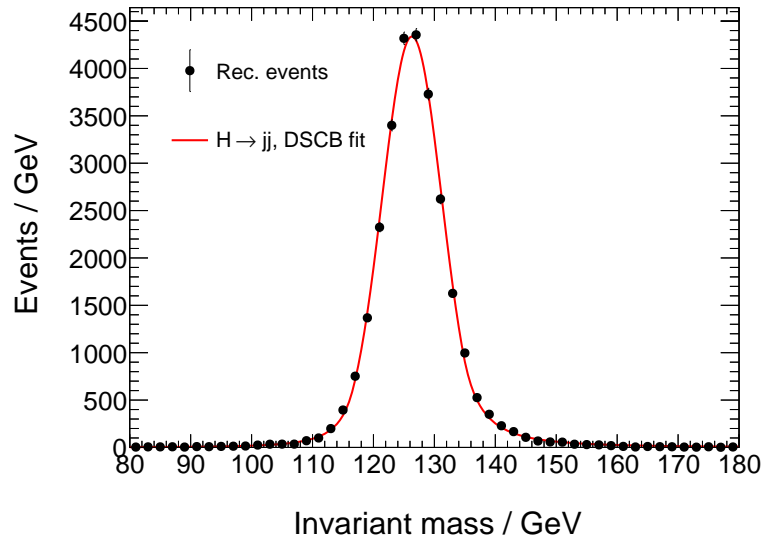


Figure 1.45: Reconstructed invariant mass of two jets using $H \rightarrow gg$ process. The fitted Higgs mass is 126.32 ± 0.04 GeV, $\sigma(m_{jj}) = 4.90 \pm 0.04$ GeV.

22] using gaseous medium, and the analog HCAL (AHCAL) with plastic scintillator tiles [18–21]. These technical routes represent different philosophies in the balance of spatial granularity, energy response, linearity, and integration complexity. The following subsections present a comparative analysis of these candidate technologies based on prototype development and beam test results which demonstrated remarkable progress in high-granularity hadronic shower imaging.

1.6.1 Study of SDHCAL

Concept

Motivated by the excellent efficiency, high homogeneity and fine lateral segmentation that gaseous detectors can provide, the concept of semi-digital HCAL (SDHCAL) is proposed aiming for the future colliders. In contrast to glass or plastic scintillator tiles, the lateral segmentation of gaseous devices is determined by the readout electronics, rather than the detector segmentation itself. In addition, the minimum thickness of active layers is also a key issue to be addressed, since the HCAL is to be placed inside the solenoid. They also have fast timing performance, making them able to be used to perform 4D reconstruction of hadronic showers, i.e. 3D spatial and 1D temporal. Such reconstruction can resolve hadronic showers from different particles and identify delayed neutrons with higher efficiency, which ultimately improves the performance of energy response.

To achieve excellent resolution in the energy measurement of hadronic showers, a binary readout of the gaseous detector is the simplest and most effective approach. However, a lateral segmentation of a few millimetres is needed to ensure good linearity and to resolve energy deposition. Such a lateral segmentation leads to a huge number of electronic channels resulting in a complicated read-out system design and excessive power consumption. A cell size of 1×1 cm² is found to be a good compromise that still provides a good resolution at moderate energy. However, simulation studies show that saturation effects are expected to show up at higher energy (>40 GeV). This happens when many particles cross a single cell at the centre of a hadronic shower. To reduce these effects, multithreshold electronics (semi-digital) readout is chosen to improve the energy resolution by utilizing the particle density information. These elements were behind the development of an SDHCAL.

Even with a 1×1 cm² lateral granularity of the read-out system, the number of electronic channels is still large. This has two important consequences: for one thing, the high power consumption and results in increasing temperature, which affects the performance of the active layers; for the other, the number of service cables needed to power and read out these channels also increases. These two aspects can degrade the performance of the HCAL if they are not addressed properly.[34]

The SDHCAL is a sampling calorimeter which uses stainless steel as the absorber and glass resistive plate chambers (GRPC) as the sensitive medium, and is designed to be as compact as possible with its mechanical structure being part of the absorber. The GRPC and the read-out electronics are conceived to achieve minimal dead regions [13]. This design renders the SDHCAL optimal for the application of the PFA techniques [1, 2, 35]. To have more detailed studies of the performance of SDHCAL, a prototype was designed and commissioned, and beam test experiments were carried out at the PS and SPS facilities of CERN.

Prototype

The SDHCAL prototype is comprised of 48 active layers. Each layer is equipped with a 1×1 m² GRPC and an active sensor unit (ASU) of the same size hosting on the one side in contact with the GRPC, pick-up pads of 1×1 cm² size each and 144 HARDROC2 ASICs [36] on the other side. The GRPC and the ASU are assembled within a cassette made of two stainless steel plates, both of which have a thickness of 2.5 mm. The 48 cassettes are inserted into a self-supporting mechanical structure made of 49 plates, each 15 mm thick, of the same material as the cassettes, bringing the total absorber thickness to 20 mm/layer. The gap between two consecutive plates is 13 mm, which allows the insertion of one cassette with a thickness of 11 mm. In total, the SDHCAL represents approximately 6 interaction lengths (λ_I). The HARDROC2 ASIC has 64 channels to read out 64 pick-up pads. Each channel has three parallel digital circuits whose parameters can be configured to provide 2-bit encoded information per channel. This indicates whether the charge seen by each pad has passed any of the three different thresholds associated with each digital circuit. This multi-threshold readout is used to improve the energy reconstruction of hadronic showers at high energies (> 30 GeV), compared to the simple binary readout mode as explained in Reference [37].

Test Beam

In 2012, using the beams provided by the SPS facility at CERN, the performance of the SDHCAL prototype was studied in the energy range above 10 GeV [37]. To study its performance under different beam conditions and at lower energy points, the SDHCAL prototype was exposed to hadrons at both the SPS and the PS facilities in 2015. It was first exposed to π^- beams of (3, 4, 5, . . . , 11) GeV at the PS facility and then to positively charged hadrons of (10, 20, 30, . . . , 80) GeV at the SPS facility. At both beamlines, about 10, 000 events were collected at each energy point.

Energy reconstruction and resolution

Based on the information of the number of hits belonging to first threshold (NHit1), second threshold (NHit2) and third threshold (NHit3), the total energy of the hadronic shower can be reconstructed by

$$E_{\text{rec}} = \alpha \cdot \text{NHit1} + \beta \cdot \text{NHit2} + \gamma \cdot \text{NHit3}, \quad (1.3)$$

as described in Reference [37], where α , β and γ are the weight factors parametrised as the second order polynomials of the total number of hits, $\text{NHit} = \text{NHit1} + \text{NHit2} + \text{NHit3}$:

$$\alpha = \alpha_1 + \alpha_2 \cdot \text{NHit} + \alpha_3 \cdot \text{NHit}^2, \quad (1.4)$$

$$\beta = \beta_1 + \beta_2 \cdot \text{NHit} + \beta_3 \cdot \text{NHit}^2, \quad (1.5)$$

$$\gamma = \gamma_1 + \gamma_2 \cdot \text{NHit} + \gamma_3 \cdot \text{NHit}^2. \quad (1.6)$$

The nine parameters $\alpha_{1,2,3}$, $\beta_{1,2,3}$ and $\gamma_{1,2,3}$ are obtained from a part of the data samples of a few energy points by minimising

$$\chi^2 = \sum_{i=1}^N \frac{(E_{\text{beam}}^i - E_{\text{reco}}^i)^2}{\sigma_i^2}, \quad (1.7)$$

as described in Reference [37], where E_{beam}^i denotes the beam energy and E_{reco}^i is the reconstructed energy; N is the total number of events and $\sigma_i = \sqrt{E_{\text{beam}}^i}$, where the choice of $\sigma = \sqrt{E_{\text{beam}}}$ is motivated by the fact that the expected energy resolution is approximately given by the stochastic term $\sigma/E_{\text{beam}} = \alpha/\sqrt{E_{\text{beam}}}$.

Based on pion test beam data collected at CERN SPS and PS with energy ranging from 3 to 80 GeV, energy linearity and resolution of the prototype are obtained, as shown in Figure 1.46. Apparently, the energy linearity is within about 4%, and the energy resolution for pion beam is $65\%/\sqrt{E} \oplus 2.5\%$. [15]

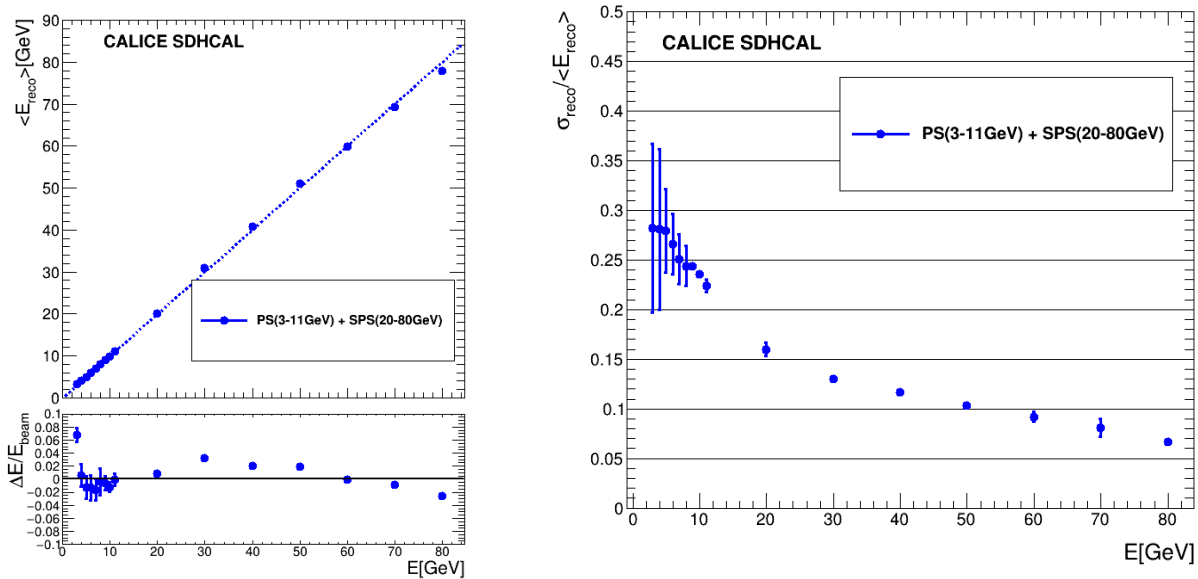


Figure 1.46: Energy linearity (left plot) and energy resolution (right plot) using all the test beam data collected at CERN with PS and SPS [15].

1.6.2 Study of AHCAL

Considering the performance, maturity and cost, a feasible solution is to develop AHCAL based on plastic scintillators. Two AHCAL prototypes are built and extensively studied within the CALICE collaboration [18–21, 38, 39].

As the baseline HCAL design in CEPC CDR, a huge amount of simulation studies were performed to address optimal design such as absorber and scintillator thickness, sampling layer and cell size with respect to physics performance [38, 39]. AHCAL technological prototype with a size of $72 \times 72 \times 120 \text{ cm}^3$ (USTC, SJTU and IHEP). It has 40 layers, each layer has 324 (18×18) plastic scintillators, each scintillator couples with a SiPM mounted on PCB. The prototype has a total of 12960 readout channels and has been successfully tested using CERN SPS and PS beams in 2022 and 2023.

Sensitive unit

A single sensitive unit is composed of a scintillator tile and a SiPM. The $40 \times 40 \times 3 \text{ mm}^3$ scintillator tile is designed with a $5.5 \times 5.5 \times 1.1 \text{ mm}^3$ groove at the bottom to accommodate SiPM, as shown in Figure 1.47a. Moreover, a LED is also positioned in the groove adjacent to the SiPM for calibration. The scintillator tiles are produced using a cost-effective injection molding technique. Subsequently, the scintillator tile is wrapped with ESR, as shown in Figure 1.47b. An automated batch test platform has been designed with 144 SiPM (HPK S13360-3025PE) mounted on PCB. About 15000 plastic scintillator tiles have been tested using ^{90}Sr radiative source. The measured light yield, corrected for the set-up response non-uniformity, is around 12.9 pe/MIP. About 91.6% of scintillators are qualified within 10% of light yield window which assures the uniform light yield of scintillators to be used for AHCAL prototype [40]. For the AHCAL prototype, SiPM (HPK S14160-1315PS) with higher PDE is placed in the groove to collect the fluorescence light. A typical response of the sensitive unit to MIP is shown as Figure 1.47c. The light yield of this unit was approximately 17 pe/MIP. The non-uniformity was approximately 6.7%.

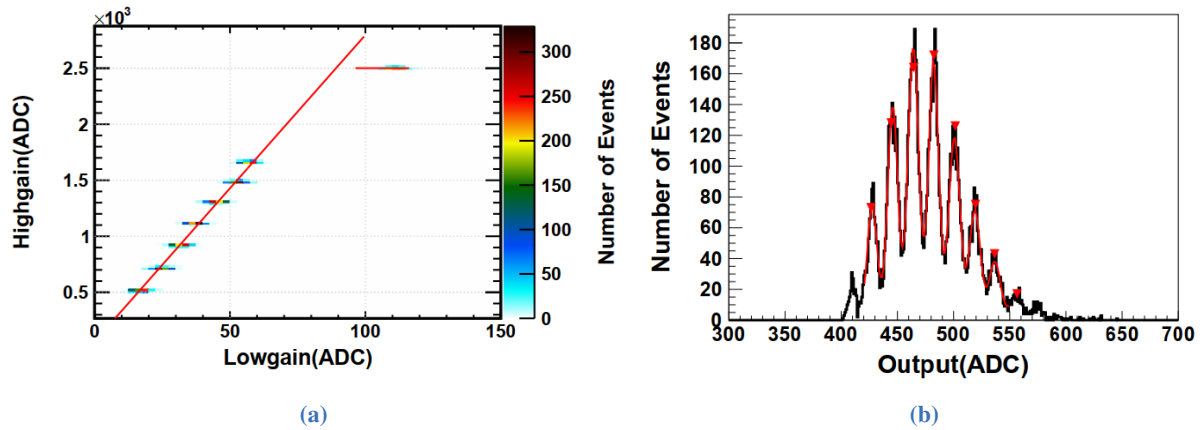


Figure 1.49: (a) Low and high gain calibration for a single channel. (b) LED spectrum of a single channel.

both 2 mm thick. This thickness ensures the stiffness of the cassette while maintaining portability. The scintillator tile, wrapped with ESR, has a thickness of 3.5 mm, while the PCB has a thickness of 2.5 mm. Additionally, a 4 mm space is designed for the electronic parts, providing a tolerance of 1 mm. The total thickness of the cassette is 14 mm. As shown in Figure 1.50(c), the scintillator tiles which glued on HBUs were placed in the steel cassette. After assembling the 40 cassettes into the structure, the whole AHCAL prototype was shown in Figure 1.51.

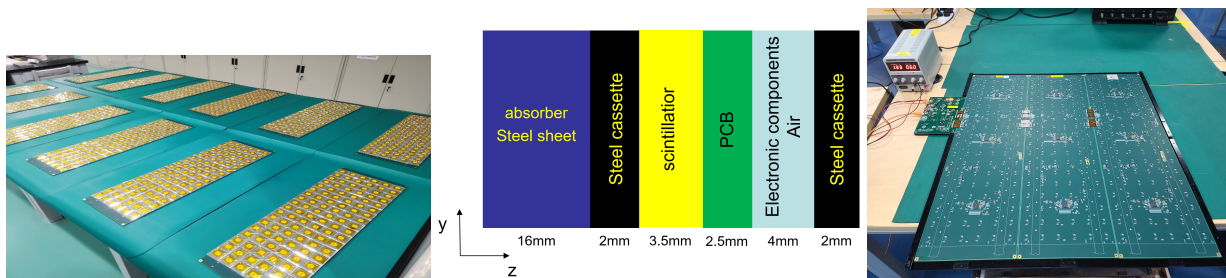


Figure 1.50: The plastic scintillators glued on HBU (left). A schematic cross-section of the AHCAL prototype (middle). The steel cassette assembled with three HBUs and the DIF board (right)

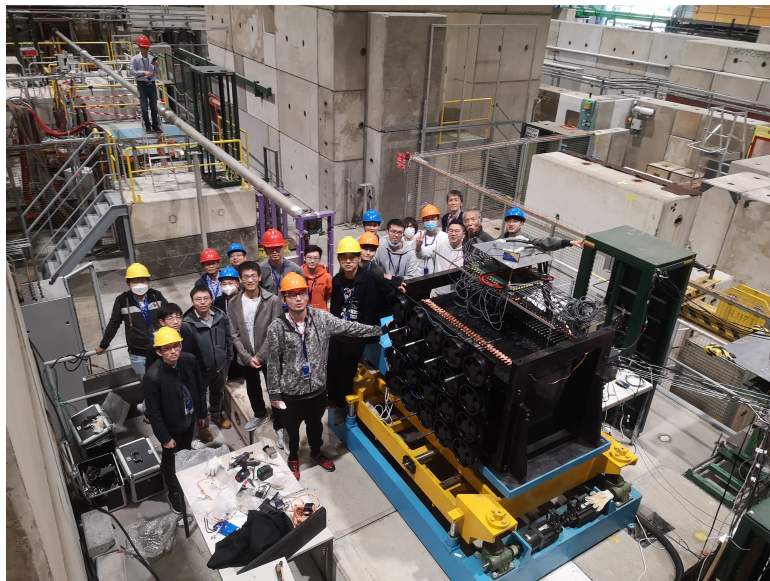


Figure 1.51: AHCAL prototype at CERN beamline with a group of colleagues from China, Japan and Israel.

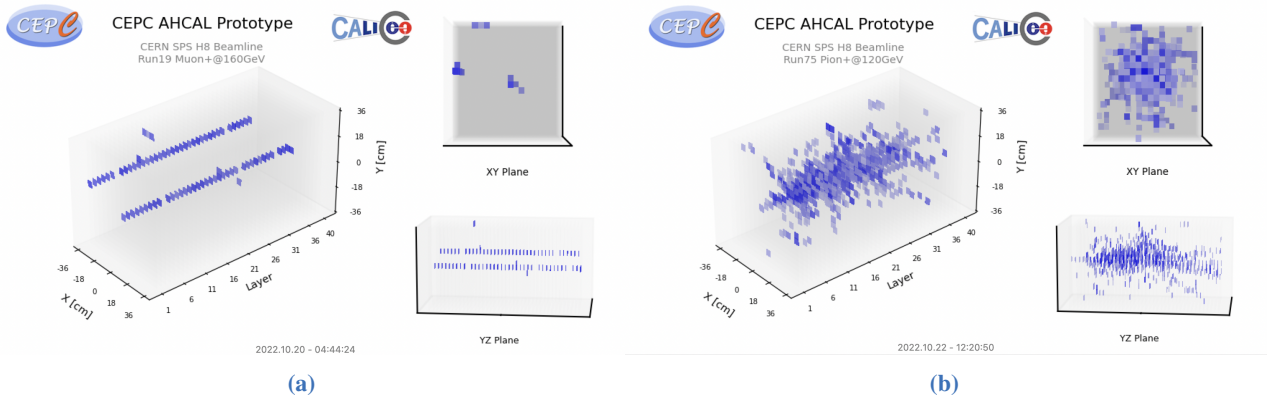


Figure 1.52: (a) AHCAL event display of two 160 GeV muon events from CERN SPS beamline. (b) AHCAL event display of a 120 GeV pion event from CERN SPS.

Beam Test and Performance

To study the performance of the AHCAL prototype, three beam tests have been carried out at CERN SPS H4, H2 and PS beamlines. About 65 millions events collected, including muons, electrons and negative pions with wide energy range from a few GeV to hundreds GeV, to study response of AHCAL prototype to high-energy particles. The event display of two 160 GeV muon and a 120 GeV pion are shown in Figure 1.52a and Figure 1.52b, respectively. Detailed studies have been performed using test beam samples, advanced machine learning methods (eg. residual neural network, graph neural network) are introduced to improve particle identification, and to obtain clean pion hadron samples with high purity [41]. The energy response linearity and energy resolution of the AHCAL prototype have been studied using high-energy pions events, as shown in Figure 1.53a and 1.53b respectively. The measured energy linearity is better than 1.5%, and the fitted energy resolution is about $56.2\%/\sqrt{E} \pm 2.5\%$ [39].

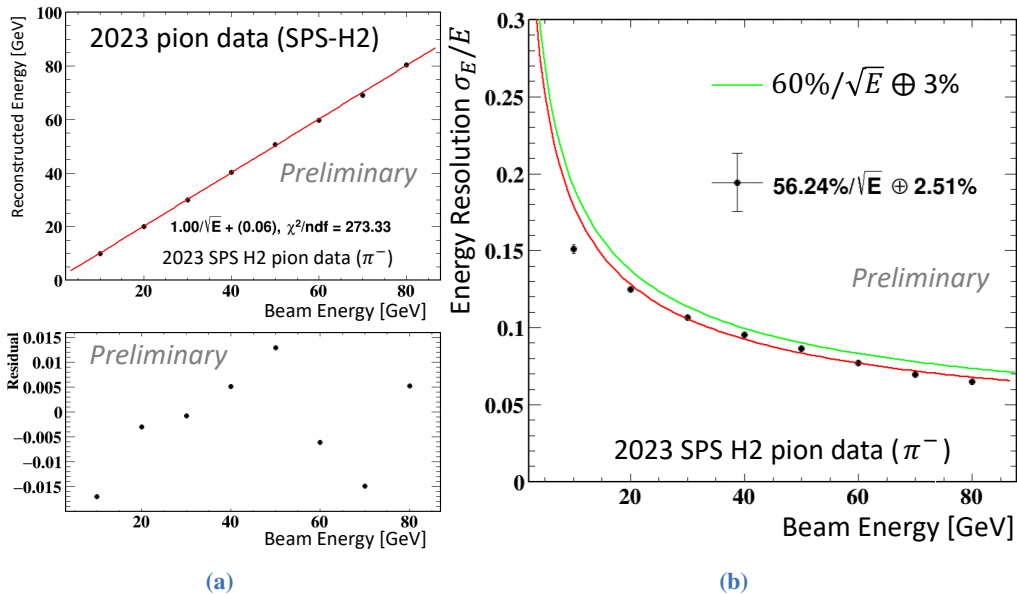


Figure 1.53: Measured energy linearity (a) and energy resolution (b) of the AHCAL prototype using high energy negative pions.

Further improvement

In the initial studies, a standard energy reconstruction technique based on calibrated sub - detector energy sums was employed. However, this method has limitations in accurately resolving hadronic energies due to the complex nature of

hadronic showers. Hadronic showers in calorimeters are characterized by a significant amount of energy loss through processes like nuclear interactions, which are difficult to precisely account for with a simple summation approach.

This algorithm takes advantage of the high granularity of the detectors, using local energy density information. Studies, such as those using the combined electromagnetic and hadronic calorimeter systems of the CALICE collaboration (e.g., the silicon - tungsten electromagnetic calorimeter (Si - W ECAL) and the scintillator - SiPM based AHCAL), have shown that the software compensation - based algorithm can improve the hadronic energy resolution by up to 30% compared to the standard reconstruction [42, 43]. When operated in hadron beams at CERN and Fermilab, the combined system data demonstrated comparable energy resolutions to those achieved for data with showers starting only in the AHCAL. This success indicates the effectiveness of the algorithm in handling the complex energy deposition patterns in hadronic showers.

1.7 Summary and future plan

The CEPC's Hadronic Calorimeter (HCAL) aims to precisely measure hadronic jets energy with high resolution and hermetic coverage, which is crucial for Higgs, electroweak and flavor physics studies. The baseline design, GS-HCAL, uses high density GS and SiPMs. It has a barrel and two endcaps, with a total of about 5.22 million cells, and is designed for PFA. The single layer structure consists of alternating glass scintillator cells and steel absorber plates, the barrel and endcap geometries are carefully designed for mechanical stability and efficient particle detection.

Past R&D efforts have focused on various aspects. High performance GFO glass have been developed, with studies on light yield, attenuation length, and radiation resistance. SiPMs have been selected as photon detectors, and efforts are ongoing to suppress their dark noise. Simulation studies have characterized the performance of the GS-HCAL, and a prototype is being developed for testing. Alternative solutions such as (S)DHCAL and AHCAL have also been explored, providing different and feasible approaches to hadronic calorimetry.

Looking ahead, several key steps are needed to meet the detector design requirements. For the GS-HCAL, the constant term in the energy resolution needs to be further reduced below 3%. This can be achieved through calibration and reconstruction improvements, such as developing more sophisticated energy weighting and compensation algorithms, implementing position dependent light collection efficiency corrections, and applying machine learning techniques to enhance energy reconstruction.

In terms of components, continuous research on GS should aim to further optimize their performance, especially in increasing the light yield and improving the attenuation length. For SiPMs, with the advancement of technology, more optimized devices are expected to emerge. Collaboration with domestic partners is essential to reduce costs while maintaining high performance.

The development of the readout electronics is crucial. A customized front-end electronics solution is needed to meet the requirements of SiPMs and the HCAL prototype. This should consider factors like charge dynamic range, timing resolution, and power consumption. As the R&D progresses, the HCAL electronics will be integrated into the whole CEPC electronics system.

Finally, extensive test and study of the prototypes, both the mini-prototype and the full-scale one, is necessary. Beam tests at CERN or alternative CSNS proton beam facility will help validate the design and performance. These tests will provide valuable data for further improvements, ensuring that the HCAL can meet the stringent requirements of the CEPC physics program and contribute to significant discoveries in high energy physics.

1.8 Cost table and justification

The cost of the HCAL is mainly determined by the total expense of the GS, SiPMs, and related readout electronics. Given that the HCAL detector has approximately 5.3 million cells and channels, its major components are listed as follows:

- Glass scintillators: there are 5.30 million cells, the cost of the glass scintillator is approximately 0.5 CHF/cc).
- SiPMs: 1 SiPM per GS cell, 5.3 million pieces. Currently, the cost of a SiPM is about 3 CHF per piece. With the advancement of massive production and maturing technology, it is expected that the cost of SiPMs will be further

reduced to about 1.25 CHF per piece.

- Electronics (FEE): Consisting of 5.3 million channels per cell, the cost of each channel is about 2.5 CHF.
- Mechanics: Comprising one Barrel and two Endcaps, including absorbers, active layers, supports, toolings, and cooling pipes.
- Assembly and installation.

Since the core components, GS and SiPMs, can be produced by domestic companies, it is essential to collaborate with domestic partners for research and development. This cooperation aims to create high performance and low cost alternative products.

Currently, each part of cost is estimated based on quotes offered by at least three different suppliers. The total cost of HCAL is 68267 kCHF if not include the cost of back-end electronics, some details listed in Table 1.9. It is quite confidence to achieve better performance glass scintillator and SiPM with low price in the future.

Table 1.9: HCAL cost breakdown

System	Cost(kCHF)
Hadron calorimeter	68267
Gass scintillator	39750
SiPMs	6625
Electronics(FEE)	13515
Mechanics	6389
Assembly and installation(3%)	1988
Extra cost for back-end electronics	8550

References

- [1] J.-C. Brient. “Improving the jet reconstruction with the particle flow method: An introduction”. In: *Calorimetry in particle physics. Proceedings, 11th International Conference, CALOR 2004, Perugia, Italy. 2004.*
- [2] M.A. Thomson. “Particle flow calorimetry and the PandoraPFA algorithm”. In: *NIMA* 611 (2009), pp. 25–40. doi: [10.1066/j.nima.2009.09.009](https://doi.org/10.1066/j.nima.2009.09.009).
- [3] Manqi Ruan and Henri Videau. “Arbor, a new approach of the Particle Flow Algorithm”. In: *International Conference on Calorimetry for the High Energy Frontier*. 2013, pp. 316–324. arXiv: [1403.4784](https://arxiv.org/abs/1403.4784) [[physics.ins-det](https://arxiv.org/abs/1403.4784)].
- [4] S. Lee et al. “Hadron detection with a dual-readout fiber calorimeter”. In: *Nuclear Instruments and Methods in Physics Research Section A* 866 (2017), p. 76.
- [5] N. Akchurin et al. “Performance of a dual-readout calorimeter for high-energy physics experiments”. In: *Nuclear Instruments and Methods in Physics Research Section A* 912 (2018), pp. 1–10. doi: [10.1016/j.nima.2018.01.001](https://doi.org/10.1016/j.nima.2018.01.001).
- [6] A. Cardini et al. “Tests of a dual-readout fiber calorimeter with SiPM light sensors”. In: *Nuclear Instruments and Methods in Physics Research Section A* 899 (2018), pp. 52–60. doi: [10.1016/j.nima.2018.04.075](https://doi.org/10.1016/j.nima.2018.04.075).
- [7] R. Wigmans. “Advances in dual-readout calorimetry for future colliders”. In: *Reviews of Modern Physics* 91 (2019), p. 045003. doi: [10.1103/RevModPhys.91.045003](https://doi.org/10.1103/RevModPhys.91.045003).
- [8] IDEA Collaboration. “Dual-readout calorimetry for the IDEA detector at future e^+e^- colliders”. In: *European Physical Journal C* 80 (2020), p. 115. doi: [10.1140/epjc/s10052-020-7671-x](https://doi.org/10.1140/epjc/s10052-020-7671-x).
- [9] M. Antonello et al. “Energy resolution and linearity of a dual-readout calorimeter prototype”. In: *Journal of Instrumentation* 17 (2022), P03014. doi: [10.1088/1748-0221/17/03/P03014](https://doi.org/10.1088/1748-0221/17/03/P03014).
- [10] CALICE Collaboration. CALICE Wikipage. URL: <https://twiki.cern.ch/twiki/bin/view/CALICE/>.

- [11] DRD6 Calorimetry Collaboration. *Detector R&D Collaboration for Calorimeters (DRD6)*. <https://greybook.cern.ch/experiment/detail?id=DRD6>. CERN Greybook Entry, Accessed: April 2025. 2025.
- [12] DRD6 Calorimetry Collaboration. *DRD 6: Calorimetry*. Tech. rep. DRDC-P-DRD6. CERN Document Server, Accessed: April 2025. CERN, 2023. URL: <https://cds.cern.ch/record/2886494>.
- [13] G. Baulieu et al. “Construction and commissioning of a technological prototype of a high-granularity semi-digital hadronic calorimeter”. In: *JINST* 10.10 (2015), P10039. DOI: [10.1088/1748-0221/10/10/P10039](https://doi.org/10.1088/1748-0221/10/10/P10039). arXiv: [1506.05316](https://arxiv.org/abs/1506.05316) [physics.ins-det].
- [14] M. Chefdeville et al. “Analysis of Testbeam Data of the Highly Granular RPC-Steel CALICE Digital Hadron Calorimeter and Validation of Geant4 Monte Carlo Models”. In: *JINST* 14 (2019), P03017. DOI: [10.1088/1748-0221/14/03/P03017](https://doi.org/10.1088/1748-0221/14/03/P03017). arXiv: [1901.08818](https://arxiv.org/abs/1901.08818) [physics.ins-det].
- [15] D. Boumediene et al. “Energy reconstruction of hadronic showers at the CERN PS and SPS using the Semi-Digital Hadronic Calorimeter”. In: *JINST* 17.07 (2022), P07017. DOI: [10.1088/1748-0221/17/07/P07017](https://doi.org/10.1088/1748-0221/17/07/P07017). arXiv: [2202.09684](https://arxiv.org/abs/2202.09684) [physics.ins-det].
- [16] V. Buridon et al. “First results of the CALICE SDHCAL technological prototype”. In: *JINST* 11.04 (2016), P04001. DOI: [10.1088/1748-0221/11/04/P04001](https://doi.org/10.1088/1748-0221/11/04/P04001). arXiv: [1602.02276](https://arxiv.org/abs/1602.02276) [physics.ins-det].
- [17] Roman Pöschl. “Recent results of the technological prototypes of the CALICE highly granular calorimeters”. In: *Nucl. Instrum. Meth. A* 958 (2020). Ed. by Manfred Krammer et al., p. 162234. DOI: [10.1016/j.nima.2019.05.075](https://doi.org/10.1016/j.nima.2019.05.075). arXiv: [1904.02825](https://arxiv.org/abs/1904.02825) [physics.ins-det].
- [18] CALICE Collaboration. “Performance of the Analogue Hadron Calorimeter with SiPM readout”. In: *Nuclear Instruments and Methods in Physics Research A* 896 (2018), pp. 24–41.
- [19] CALICE Collaboration. “Construction and Commissioning of the CALICE Analog Hadron Calorimeter Prototype”. In: *JINST* 11 (2016). Detailed description of the AHCAL prototype construction and performance., P05001. DOI: [10.1088/1748-0221/11/05/P05001](https://doi.org/10.1088/1748-0221/11/05/P05001).
- [20] F. Sefkow et al. “Performance of the Highly Granular CALICE AHCAL in Beam Tests”. In: *Proceedings of the IEEE NSS/MIC*. Beam test results and energy resolution studies. 2018. arXiv: [1811.07991](https://arxiv.org/abs/1811.07991) [physics.ins-det].
- [21] DESY CALICE Group. *Development of the Scintillator-Based Analog Hadron Calorimeter for the ILD Detector*. Tech. rep. Technical report on the AHCAL design and SiPM-on-tile readout. DESY, 2015.
- [22] et al. Bressler Shikma. “Novel Resistive-Plate WELL sampling element for (S)DHCAL”. In: *Nuclear Instruments and Methods in Physics Research Section A: Accelerators, Spectrometers, Detectors and Associated Equipment* 958 (2020), p. 162861. DOI: [10.1016/j.nima.2019.162861](https://doi.org/10.1016/j.nima.2019.162861).
- [23] Crystal Clear Collaboration. *Crystal Clear Collaboration*. 2024. URL: <https://crystalclearcollaboration.web.cern.ch/> (visited on 05/01/2024).
- [24] X.Y. Sun et al. “Tunable valence state and scintillation performance of dense Ce³⁺-doped borosilicate glasses prepared in ambient atmosphere”. In: *J. Mater. Chem. C* 12 (2024), p. 11149.
- [25] A. Phunpueok et al. “Comparison of Scintillation Light Yield of CWO and BGO Single Crystals for Gamma Ray Detection”. In: *Applied Mechanics and Materials* 901 (2019), pp. 89–94.
- [26] V. Dormenev et al. “Multipurpose Ce-doped Ba-Gd silica glass scintillator for radiation measurements”. In: *Nucl. Instrum. Methods Phys. Res. A* 1015 (2021), p. 165762.
- [27] Z.H. Hua et al. “Light attenuation and loss in Ce³⁺-doped dense glass scintillator”. In: *Nucl. Instrum. Methods Phys. Res. A* 1072 (2025), p. 170182.
- [28] Yingyi Liu et al. “Physical design of the APEP beam line at CSNS”. In: *Nuclear Instruments and Methods in Physics Research Section A: Accelerators, Spectrometers, Detectors and Associated Equipment* 1042 (2022), p. 167431. ISSN: 0168-9002. DOI: <https://doi.org/10.1016/j.nima.2022.167431>.

- [29] *The Phase-2 Upgrade of the CMS Endcap Calorimeter*. Tech. rep. Geneva: CERN, 2017. DOI: [10.17181/CERN.IV8M.1JY2](https://doi.org/10.17181/CERN.IV8M.1JY2). URL: <https://cds.cern.ch/record/2293646>.
- [30] *The Phase-2 Upgrade of the CMS Barrel Calorimeters*. Tech. rep. This is the final version, approved by the LHCC. Geneva: CERN, 2017. URL: <https://cds.cern.ch/record/2283187>.
- [31] M. Janecek. “Reflectivity Spectra for Commonly Used Reflectors”. In: *IEEE Transactions on Nuclear Science* 59.3 (2012). PISCATAWAY: IEEE, pp. 490–497. ISSN: 0018-9499. DOI: [10.1109/TNS.2012.2183385](https://doi.org/10.1109/TNS.2012.2183385).
- [32] G. Drake et al. “A Digital Hadron Calorimeter with Resistive Plate Chambers for the Linear Collider”. In: *International Journal of Modern Physics A* (2005). DOI: [10.1142/S0217751X05027746](https://doi.org/10.1142/S0217751X05027746). URL: <https://ui.adsabs.harvard.edu/abs/2005IJMPA..20.3830D/abstract>.
- [33] B. Bilki et al. “Digital Hadron Calorimetry”. In: *2021 IEEE Nuclear Science Symposium and Medical Imaging Conference, NSS/MIC 2021*. 2021. DOI: [10.1109/NSS/MIC44867.2021.9875821](https://doi.org/10.1109/NSS/MIC44867.2021.9875821). URL: <https://gcris.ktun.edu.tr/handle/20.500.13091/4426>.
- [34] Mingyi Dong et al. “CEPC Conceptual Design Report: Volume 2 - Physics & Detector”. In: (Nov. 2018). Ed. by João Barreiro Guimarães da Costa et al. arXiv: [1811.10545](https://arxiv.org/abs/1811.10545) [hep-ex].
- [35] Manqi Ruan. *Arbor, a new approach of the Particle Flow Algorithm*. 2014. arXiv: [1403.4784](https://arxiv.org/abs/1403.4784) [physics.ins-det]. URL: <https://arxiv.org/abs/1403.4784>.
- [36] Frederic Dulucq et al. “HARDROC: Readout chip for CALICE/EUDET Digital Hadronic Calorimeter”. In: *IEEE Nuclear Science Symposium & Medical Imaging Conference*. 2010, pp. 1678–1683. DOI: [10.1109/NSSMIC.2010.5874060](https://doi.org/10.1109/NSSMIC.2010.5874060).
- [37] The CALICE collaboration. “First results of the CALICE SDHCAL technological prototype”. In: *Journal of Instrumentation* 11.04 (2016), P04001. DOI: [10.1088/1748-0221/11/04/P04001](https://doi.org/10.1088/1748-0221/11/04/P04001). URL: <https://dx.doi.org/10.1088/1748-0221/11/04/P04001>.
- [38] Yukun Shi et al. “Design and optimization of the CEPC scintillator hadronic calorimeter”. In: *Journal of Instrumentation* 17.11 (2022), P11034. DOI: [10.1088/1748-0221/17/11/P11034](https://doi.org/10.1088/1748-0221/17/11/P11034). URL: <https://dx.doi.org/10.1088/1748-0221/17/11/P11034>.
- [39] Jianbei Liu et al. “CALICE scintillator-SiPM calorimeter prototypes: R&D highlights and beamtests”. In: *Nucl. Instrum. Methods Phys. Res. A* 1072 (2025), p. 170191. ISSN: 0168-9002. DOI: <https://doi.org/10.1016/j.nima.2024.170191>.
- [40] Yanyun Duan et al. “Scintillator Tile Batch Test of CEPC AHCAL”. In: *Journal of Instrumentation* 17 (2022), P05006. DOI: [10.1088/1748-0221/17/05/P05006](https://doi.org/10.1088/1748-0221/17/05/P05006). arXiv: [2111.03660](https://arxiv.org/abs/2111.03660) [physics.ins-det].
- [41] Siyuan Song et al. “Study of residual artificial neural network for particle identification in the CEPC high-granularity calorimeter prototype”. In: *Journal of Instrumentation* 09 (2024), P04033. DOI: [10.1088/1748-0221/09/04/P04033](https://doi.org/10.1088/1748-0221/09/04/P04033). arXiv: [2310.09489](https://arxiv.org/abs/2310.09489) [physics.ins-det].
- [42] Y. Israeli. “Energy Reconstruction of Hadrons in highly granular combined ECAL and HCAL systems”. In: *Journal of Instrumentation* 13.05 (2018), p. C05002. DOI: [10.1088/1748-0221/13/05/C05002](https://doi.org/10.1088/1748-0221/13/05/C05002). arXiv: [1803.05232](https://arxiv.org/abs/1803.05232) [physics.ins - det].
- [43] F. Simon. “Energy Reconstruction of Hadron Showers in the CALICE Calorimeters”. In: *arXiv preprint arXiv:0911.4575* (2009). arXiv: [0911.4575](https://arxiv.org/abs/0911.4575) [physics.ins - det].